

MASARYKOVA UNIVERZITA

Přírodovědecká fakulta

Ústav teoretické fyziky a astrofyziky

DIPLOMOVÁ PRÁCE

Brno 2022

Michaela Vítková

M A S A R Y K O V A U N I V E R Z I T A

Přírodovědecká fakulta
Ústav teoretické fyziky a astrofyziky

Měření radiálních rychlostí s využitím jódové cely

Diplomová práce

Michaela Vítková

Vedoucí diplomové práce:
Mgr. Marek Skarka, Ph.D.

Brno 2022

Bibliografický záznam

Autor: Bc. Michaela Vítková
Přírodovědecká fakulta, Masarykova univerzita
Ústav teoretické fyziky a astrofyziky

Název práce: Měření radiálních rychlostí s využitím jódové cely

Studijní program: Teoretická fyzika a astrofyzika

Směr: Astrofyzika

Vedoucí práce: Mgr. Marek Skarka, Ph.D.

Konzultant: Mgr. Marie Karjalainen, Ph.D.

Akademický rok: 2021/2022

Počet stran: ix + 52

Klíčová slova: exoplaneta, radiální rychlost, Dopplerův jev, jódová cely, viper, IRAF, Ondřejovský ešletový spektrograf

Bibliographic record

Author: Bc. Michaela Vítková
Faculty of Science, Masaryk University
Department of Theoretical Physics and
Astrophysics

Title of Thesis: Radial velocity measurements with the
iodine cell

Degree Programme: Theoretical physics and astrophysics

Field of study: Astrophysics

Supervisor: Mgr. Marek Skarka, PhD

Advisor: Mgr. Marie Karjalainen, Ph.D.

Academic Year: 2021/2022

Number of Pages: ix + 52

Keywords: exoplanet, radial velocity, Doppler effect,
iodine cell, viper, IRAF, Ondřejov echelle
spectrograph

Abstrakt

V této diplomové práci se zabývám využitím jodové cely na Ondřejovském ešeletovém spektrografu (OES) pro měření doplerovského posunu spektrálních čar hvězd a tedy jejich radiálních rychlostí. Pro zpracování dat jsem využívala program `viper` napsaný v Pythonu. Tento program se stále vyvíjí a mým úkolem bylo jej otestovat a vyladit nastavení pro použití na datech z OES. Z mé analýzy vyplývá, že je vhodné použít jen některé apertury obsahující jodové spektrum. Pro dosažení lepších výsledků je dobré použít nenormalizovaná data. Dále jsem zjistila, že použití šablony s poměrem signálu k šumu (SNR) kolem 100 je dostačující a jakýkoliv šablona s vyšším SNR dával podobné výsledky. Použití šablony s vysokým rozlišením pořízeného na jiném spektrografu (HARPS) ukázalo, že je lepší použít šablony z OES (testováno na 51 Pegasi). Náhlá změna teploty v kopuli provázená změnou seeingu má vliv na přesnost měření (testováno na σ Draconis). Data měření σ Draconis během jedné noci ukázala rozptyl 14 m/s. Dlouhodobá přesnost měření radiálních rychlostí pak byla testována na HD 182572, kdy během 175 dní byl rozptyl měření 12 m/s. U dalšího standardu, HD 10780, byl detekován trend, který nejspíše souvisí s vlastní proměnností či dvojhvězdností hvězdy. Mohlo by se dokonce jednat o exoplanetu.

Abstract

In this diploma thesis, I deal with the usage of the iodine cell on the Ondřejov Echelle Spectrograph (OES) for measuring the Doppler shift of the spectral lines of stars and, thus, their radial velocities. I used **viper**, a Python-based program, to process the data. This program is still under development, and my task was to test it and tune the setting for the usage of the data from OES. My analysis shows that it is better to use only some apertures containing the iodine spectrum. It is also better to use non-normalised data. Furthermore, I found that using a template with a signal to noise ratio (SNR) of around 100 is sufficient and a template with a higher SNR gave similar results. Using a high-resolution template taken with another spectrograph (HARPS) has shown that it is better to use a template from OES (tested on 51 Pegasi). Sudden change in the dome temperature accompanied by a change in seeing affects the accuracy of the measurement (tested on σ Draconis). The measured data of σ Draconis during one night showed a scatter of 14 m/s. The long-term accuracy of radial velocity measurements was tested on HD 182572, where the measured scatter of the radial velocities was 12 m/s within 175 days. For another standard, HD 10780, a trend in the data was detected. It is most likely related to the star's variability or possible binarity. It could even be an exoplanet.

ZADÁNÍ
DIPLOMOVÉ PRÁCE

Akademický rok: 2021/2022

Ústav:	Ústav teoretické fyziky a astrofyziky
Studentka:	Bc. Michaela Vítková
Program:	Fyzika
Specializace:	Astrofyzika

Ředitel ústavu PTF MU Vám ve smyslu Studijního a zkušebního řádu MU určuje diplomovou práci s názvem:

Název práce:	Měření radiálních rychlostí s využitím jódové cely
Název práce anglicky:	Radial velocity measurements with the iodine cell
Jazyk závěrečné práce:	angličtina

Oficiální zadání:

Přesné měření radiálních rychlostí exoplanet je velmi složitý úkol. Jednou z nejlepších možností jak eliminovat vliv okolních podmínek na měření a řádově zlepšit přesnost je použít tzv. jódovou celou. Dostupný software pro zpracování spekter naměřených s jódovou celou je velmi složitý na instalaci a použití. Student/ka se ve své práci zaměří na pochopení principů měření s jódovou celou a na vývoj softwaru, který by byl využitelný pro spektra pořízená echelleovým spektrografem OES na Astronomickém ústavu AV ČR v Ondřejově.

Vedoucí práce:	Mgr. Marek Skarka, Ph.D.
Datum zadání práce:	27. 11. 2020
V Brně dne:	28. 2. 2022

Zadání bylo schváleno prostřednictvím IS MU.

Bc. Michaela Vítková, 14. 2. 2022

Mgr. Marek Skarka, Ph.D., 16. 2. 2022

Mgr. Dušan Hemzal, Ph.D., 16. 2. 2022

Poděkování

V první řadě bych chtěla poděkovat svému vedoucímu Marku Skarkovi za předání hodnotných zkušeností a rad, za jeho podporu, trpělivost a podněty k této práci. Také bych chtěla poděkovat mé konzultantce Marii Karjalainen a celé Ondřejovské Exoplanetární skupině za cenné rady a poskytnutá data. V neposlední řadě mé díky patří podporující rodině.

Special thanks also go to Jana Köhler and Sireesha Chamarthi for the introduction to *viper* and useful tips.

Prohlášení

Prohlašuji, že jsem svoji diplomovou práci vypracovala samostatně pod vedením vedoucího práce s využitím informačních zdrojů, které jsou v práci citovány.

Brno 16. května 2022

Podpis autora

Contents

1	Fundamenals for exoplanets exploration via Doppler method	1
1.1	History of exoplanetary research	2
1.2	Radial velocity method	3
1.2.1	Planetary orbits	3
1.2.2	Radial velocity curve	5
1.3	Echelle spectrographs	7
1.3.1	Ondřejov Echelle Spectrograph (OES)	9
1.4	Sources of radial velocity measurement errors	11
1.4.1	Influence of the instrument and the data properties	11
1.4.2	Influence of the stellar characteristics	12
1.4.3	Overall formula for the uncertainty	13
2	Methods to calculate Doppler shifts	14
2.1	Basic data reduction with IRAF	14
2.2	Wavelength calibration and RV determination	18
2.3	Cross-correlation method	19
2.4	Iodine cell method	20
2.4.1	Instrumental Profile (IP)	21
3	Setting up viper for OES data	24
3.1	Introduction to viper: Velocity an IP Estimator	24
3.2	Testing of parameters	27
3.3	Which apertures to use?	29
3.4	Impact of the template	31
3.4.1	High-resolution template	33
3.5	Observing conditions	34
3.6	Long-term stability	35
3.7	Cross-correlation with IRAF vs VIPER and iodine cell method .	36
3.8	HD 187878	37
4	Discussion and conclusions	39
	Bibliography	41

A	Input data for viper	44
B	Radial velocity	49
B.1	σ Draconis	49
B.2	51 Pegasi	50
B.3	HD 182572	50
B.4	HD 10780	51
B.5	HD 187878	52

Fundamentals for exoplanets exploration via Doppler method

The first exoplanet, 51 Pegasi b, orbiting a main-sequence star was discovered with the Doppler method. This discovery started a huge development in the field of exoplanets. The Doppler method is not the most efficient in terms of the number of discovered exoplanets since it was outshined by the transit method. Doppler method is still needed for the exoplanet confirmation and follow-up observation of transit-method discoveries. Along with astrometry, this method gives us the most important parameter of the exoplanet, its mass. For all the successful transit-method space missions applies that follow-up spectroscopic ground-based observation is important for the closer planet characterization.

In this thesis, I deal with the iodine cell method. The main advantages of this method are that the calibration of the data is taken simultaneously with the observations and getting information about the instrumental profile. The instrumental profile can influence the radial velocities results quite strongly, depending on the stability of the spectrograph.

It is possible to use iodine cell with Ondřejov Echelle Spectrograph (OES). Available software for Doppler shift calculation from iodine cell observations is rather complicated. Thanks to the cooperation between the Exoplanet group in Ondřejov and Exoplanet group at Thüringer Landessternwarte Tautenburg I was able to test `viper` software and use it on OES data.

This work is divided into four chapters. In Chapter 1 I give an overview of the history of exoplanet research, radial velocity method, sources of errors in radial velocity measurements and echelle spectrographs. In Chapter 2 I describe the methods for Doppler shift calculation and give an introduction to `viper`. In Chapter 3, the testing of `viper` is shown. The conclusions are described in Chapter 4.

1.1 History of exoplanetary research

Discussion about the existence of planets outside of the Solar system (exoplanets) had been here since ancient times, but there was no way of proving it. In the 16th century, Giordano Bruno, a supporter of heliocentrism, believed that other stars were similar to Sun and had planets (Maor, 1987).

The hunt for detection of the first exoplanet began in the 19th century, using the astrometry method. The astrometry method is based on the measurements of the star's position by observations of the star's motion on the plane of the sky. This movement is caused by the star orbiting around the common centre of gravity of the system star-planet. William Stephen Jacob concluded from observations of binary star 70 Ophiuchi that it is highly probable that this system has a third body, a planet (Jacob, 1855). The existence of this exoplanet is still not confirmed but Wittenmyer et al. (2006) concluded that there might be one or more planets. During the second half of the 20th century, Peter van de Kamp (1969) observed Barnard's Star and claimed the discovery of a planet with mass $M_p = 1.6 M_J$. In 2018 it was proposed that super-Earth with mass $M_p \geq 3.23 \pm 0.44 M_E$ orbits Barnard's star (Ribas et al., 2018). According to Lubin et al. (2021), this radial velocity signal disappeared in newer data.

At that time, astrometry was not the most accurate method, as it is very demanding on time, precise measurements and instruments. The first promising detections of exoplanets were made in the late 20th century using the radial velocity method. The first thoughts that Doppler spectroscopy could be used for detecting exoplanets were made by Otto Struve (1952) in his Proposal for a project of high-precision stellar radial velocity work, where he claims that it would be possible to detect Jupiter-mass planets orbiting close to the parent star, planets that we now call Hot Jupiters.

Later in the 20th century, progress in spectrometer technology gave rise to more powerful spectrographs. In 1993, the ELODIE spectrograph was installed at 1.93m telescope at Haute-Provence Observatory. Observed instrumental velocity error of this spectrograph was $13 \text{ m} \cdot \text{s}^{-1}$ (Baranne et al., 1996). For example, Jupiter produces a reflex motion of the Sun with the amplitude of $12.4 \text{ m} \cdot \text{s}^{-1}$ over a period of 12 years [E01]. The first exoplanet orbiting a main-sequence star, 51 Pegasi, was discovered using ELODIE (Mayor and Queloz, 1995). It was also the first exoplanet discovered using the radial velocity method. Since then, over 900 exoplanets were discovered using this method [E02]. In 2003, the HARPS spectrograph was installed on the ESO's 3.6m telescope at La Silla Observatory in Chile (Mayor et al., 2003). Long-term stability of the HARPS is $\approx 1 \text{ m} \cdot \text{s}^{-1}$ (Lovis et al., 2006). In 2017, the ESPRESSO spectrograph of ESO's Very Large Telescope (VLT) was installed at the Paranal Observatory. Radial velocity accuracy is better than $0.5 \text{ m} \cdot \text{s}^{-1}$ (Pepe et al., 2021).

1.2 Radial velocity method

The radial velocity method, also called Doppler spectroscopy, is one of many methods how to detect exoplanets. It is the second most successful method for discovering exoplanets after the transit method. To this date (May 16th, 2022), 923 exoplanets using this method were discovered, which is 18.4 % of the total number of discovered exoplanets [E02]. It is the only method that gives us a good estimate of the minimal planet mass, in combination with the transit method it gives us the absolute planet mass.

1.2.1 Planetary orbits

The star and its planet are orbiting in elliptical orbits around the common centre of gravity located at one of the focus of the ellipses. Planet's orbit is shown in Figure 1.1. In polar coordinates we can describe the ellipse (Perryman, 2018)

$$r = \frac{a(1 - e^2)}{1 + e \cos \nu}. \quad (1.1)$$

Ellipse can be also described in Cartesian coordinates

$$\frac{x^2}{a^2} + \frac{y^2}{b^2} = 1, \quad (1.2)$$

where a is semi-major axis, b is semi-minor axis and e is eccentricity. These three parameters of the ellipse are related in the following way

$$b^2 = a^2(1 - e^2). \quad (1.3)$$

The pericentre distance q and apocentre distance Q are

$$\begin{aligned} q &= a(1 - e) \\ Q &= a(1 + e). \end{aligned} \quad (1.4)$$

For a description of numerous angles in the orbit of the planet, the following terms are used: The true anomaly $\nu(t)$ is the angle between the direction of the pericentre and the actual position of the planet measured from the centre of gravity (shown in Figure 1.1 and 1.2). The eccentric anomaly, $E(t)$ is the angle that is related to the auxiliary circle of the ellipse (shown in Figure 1.1). These two parameters are related by

$$\cos \nu(t) = \frac{\cos E(t) - e}{1 - e \cos E(t)}. \quad (1.5)$$

According to the second Kepler's law, the planet does not move at a constant angular rate over the whole orbit. The mean anomaly $M(t)$ is an angle associated with imaginary mean motion around the orbit. Mean anomaly at time $t - t_p$ after going through pericentre is

$$M(t) = \frac{2\pi}{P}(t - t_p). \quad (1.6)$$

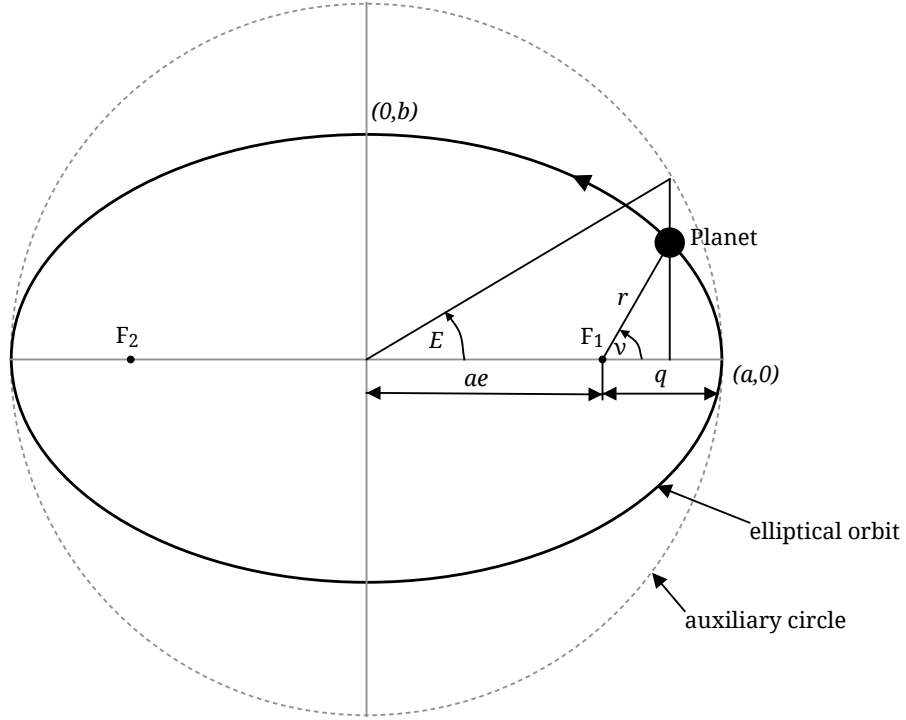


Figure 1.1: Illustration of the elliptical orbit of a planet. Focus F_1 is the system barycentre. The position of the planet in the orbit is described with the true anomaly ν (with respect to the ellipse) or the eccentric anomaly E (with respect to the auxiliary circle). Based on Perryman (2018).

The relation between the mean anomaly $M(t)$ and the eccentric anomaly $E(t)$ can be derived

$$M(t) = E(t) - e \sin E(t). \quad (1.7)$$

Using equation 1.6 we can calculate the position of an exoplanet along its orbit at any time. Equation 1.7 can be solved iteratively for E and then equation 1.5 can be used to calculate ν .

Further parameters for the planet's orbit description are inclination i , an argument of pericentre ω and longitude of ascending node Ω , these parameters are shown in Figure 1.2.

For the movement of two objects, the following relations apply

$$e_{\text{rel}} = e_* = e_{\text{p}} \quad (1.8)$$

$$P_{\text{rel}} = P_* = P_{\text{p}} \quad (1.9)$$

$$a_* : a_{\text{p}} : a_{\text{rel}} = M_{\text{p}} : M_* : (M_* + M_{\text{p}}), \quad (1.10)$$

where $a_{\text{rel}} = a_* + a_{\text{p}}$.

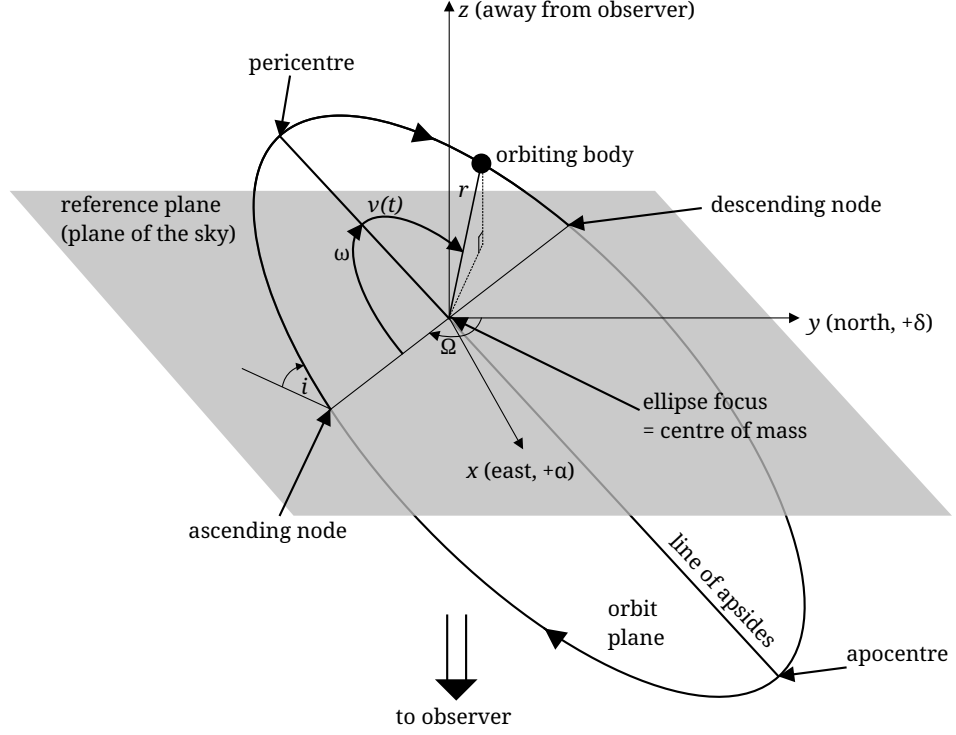


Figure 1.2: Illustration of the elliptical orbit of the planet in three dimensions. Parameters for the description of the orbit are shown. The inclination of the orbit plane i , the longitude of the ascending node Ω , the object's argument of pericentre (relative to ascending node) ω , object's position along the orbit described by the true anomaly ν . Based on Perryman (2018).

1.2.2 Radial velocity curve

In vast majority of exoplanetary systems, the only movement of a star that we can measure is in the radial direction, i.e., the radial velocity. We can derive this as the star's z -coordinate from trigonometry (Perryman, 2018)

$$z = r(t) \sin i \sin(\omega + \nu), \quad (1.11)$$

where $r(t)$ is the distance from the barycentre. Simply deriving equation 1.11 we obtain

$$v_r = \dot{z} = \sin i [\dot{r} \sin(\omega + \nu) + r \dot{\nu} \cos(\omega + \nu)]. \quad (1.12)$$

After some substitutions we get

$$v_r = K [\cos(\omega + \nu) + e \cos \omega], \quad (1.13)$$

where K is radial velocity semi-amplitude. It is given by

$$K = \frac{2\pi}{P} \frac{a_* \sin i}{(1 - e^2)^{1/2}}. \quad (1.14)$$

If we substitute a_* into the equation 1.14 from third Kepler's law

$$P^2 = \frac{4\pi^2}{GM} a_*^3, \quad (1.15)$$

where $M = \frac{M_p^3}{(M_* + M_p)^2}$, we get

$$K = \left(\frac{2\pi G}{P} \right)^{1/3} \frac{M_p \sin i}{(M_* + M_p)^{2/3}} \frac{1}{(1 - e^2)^{1/2}}. \quad (1.16)$$

In this equation, a term for mass function can be seen

$$\mathcal{M} = \frac{M_p^3 \sin^3 i}{(M_* + M_p)^2}. \quad (1.17)$$

An illustration of the radial velocity curve and semi-amplitude K is shown in Figure 1.3. From the equation 1.17 follows that with known stellar-mass we can calculate a lower limit of the exoplanet mass. For the true value of planet mass, we need to know the inclination i . This parameter we can get from other methods such as transit or astrometry.

The radial velocity method is based on measuring doppler shifts in the spectrum of stars. The principle of this method is shown in Figure 1.3. The planet and its star are orbiting around the common centre of gravity. This little wobble of the star is causing redshift when the star is going away from us and blueshift when the star is going towards us.

This gives us the ability to measure small shifts of absorption lines in stellar spectra

$$\Delta\lambda = \lambda_{\text{obs}} - \lambda_{\text{em}}. \quad (1.18)$$

It is related to velocity by the relativistic Doppler shift equation

$$\lambda_{\text{obs}} = \lambda_{\text{em}} \frac{1 + \beta \cos \theta}{\sqrt{1 - \beta^2}}, \quad (1.19)$$

where λ_{obs} , λ_{em} are observed and emitted wavelength, $\beta = v/c$ and θ is an angle relative to the observer-source direction. For $v \ll c$ and $\theta \ll \pi/2$ we can rewrite this expression into classical form and the radial velocity (RV) is

$$v_r = v \cos \theta = \frac{\Delta\lambda}{\lambda_{\text{em}}} c. \quad (1.20)$$

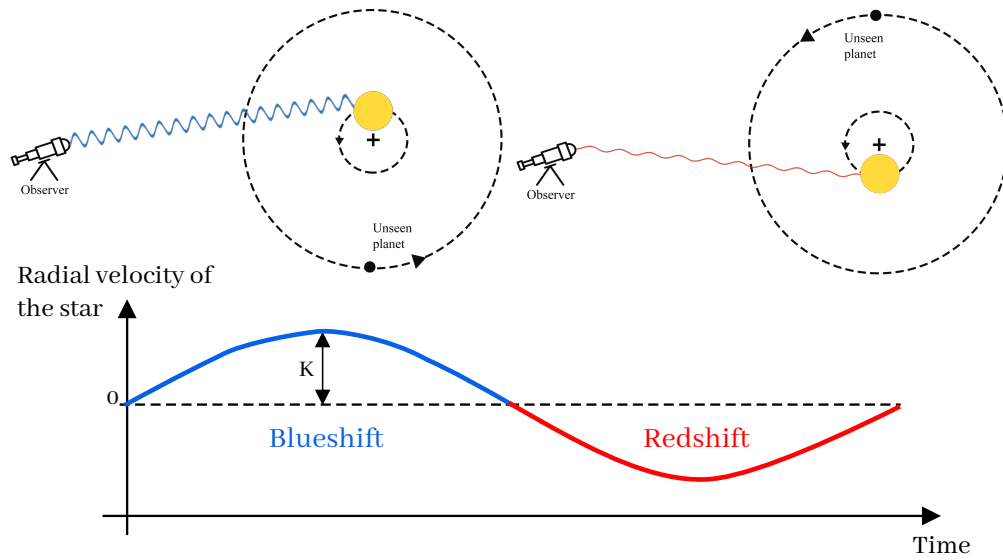


Figure 1.3: An illustration of the radial velocity method.

1.3 Echelle spectrographs

The classic design of a high-resolution spectrograph is shown in Figure 1.4 on the left. Light from a telescope is brought to a slit which is in focus and then it diverges. Light goes through a collimator and then collimated light hits the echelle grating which is a dispersing element. After the dispersion of the light,

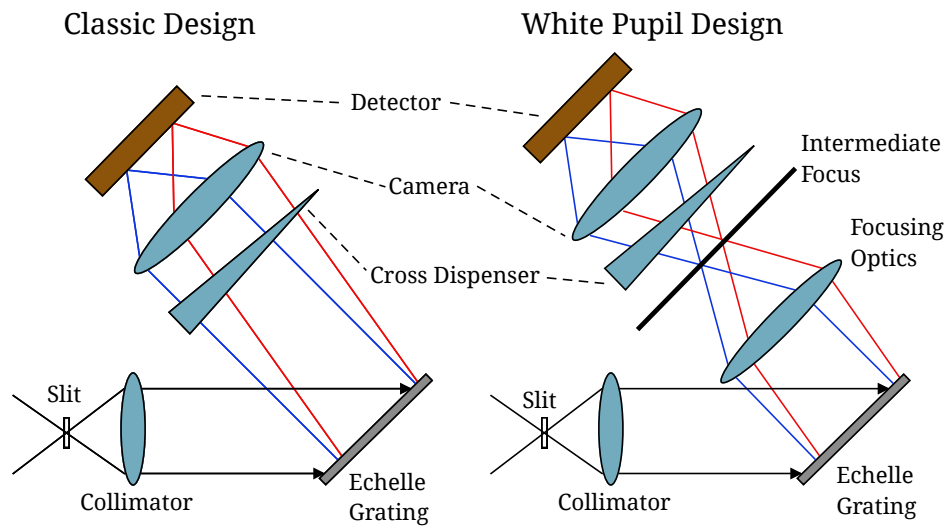


Figure 1.4: Design of the high-resolution spectrograph. A classic design is on the left. The white pupil design is on the right. Based on Hatzes (2019).

it is focused with the camera onto the detector. The camera can be either a reflective, Schmidt-type camera or a refractive, lens-based system. Spectrographs with slits generally use the refractive camera and spectrographs with fibre-optic use lens cameras.

Because the Echelle grating produces overlapping orders, it is needed to separate these orders by cross-disperser which is an element of a spectrograph that disperses the light.

One of many designs of echelle spectrographs is the white-pupil design. It is shown in Figure 1.4 on the right. This design has an additional optical element. This additional part of the design produces an intermediate focus between the grating and the cross-disperser. At this place, spectral orders are created but not separated yet and a superposition of all wavelengths appears. This results in the formation of an intermediate white-light image of the slit. Because of this additional optical element, all the subsequent parts of the spectrograph can be made smaller. Smaller parts mean a spectrograph that is easier to stabilize thermally and mechanically and also reduced price. Stray light is reduced by a spatial filter at the intermediate focus. The only disadvantage, small light loss, is a small price for all the advantages of the white-pupil design (Hatzes, 2019).

Echelle grating

The echelle grating is an essential component of a spectrograph. In Figure 1.5, the chart of a grating is shown. For each grating, the grating equation applies

$$m\lambda = d (\sin \alpha + \sin \beta), \quad (1.21)$$

where m is an order number, λ is wavelength, d is grating constant, α is incidence angle and β is angle of diffraction (shown in Figure 1.5). For order $m = 0$, there is no diffraction. From this equation, one can notice that for given λ the same solution is achieved for small m and small d or for large m and large d .

By derivating the grating equation 1.21, we obtain angular dispersion $d\beta/d\lambda$:

$$\frac{d\beta}{d\lambda} = \frac{m}{d \cos \beta}. \quad (1.22)$$

This means that higher dispersion is in higher orders. If we combine equations 1.21 and 1.22 we can eliminate the number of order and we get:

$$\frac{d\beta}{d\lambda} = \frac{\sin \alpha + \sin \beta}{\lambda \cos \beta}. \quad (1.23)$$

In the so called Littrow configuration, $\lambda = \beta = \Theta_B$, we obtain

$$\frac{d\beta}{d\lambda} = \frac{2}{\lambda} \tan \Theta_B, \quad (1.24)$$

where Θ_B is a blaze angle, which is a tilt of the groove. From this equation follows that for large angular dispersion large blaze angle is required. Typical

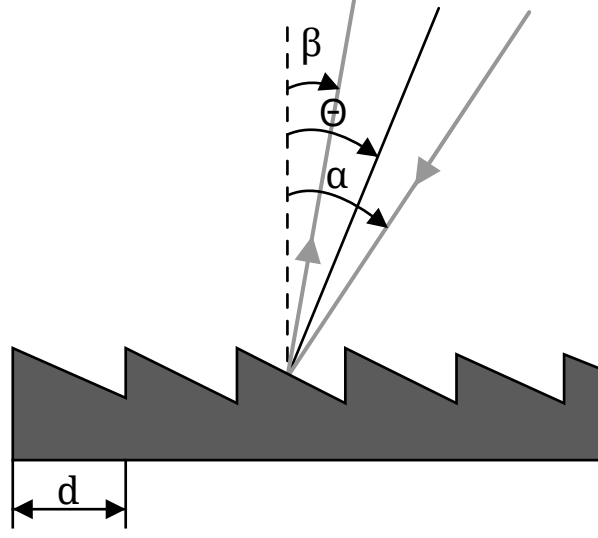


Figure 1.5: Illustration of the echelle grating. The width of a groove is marked d , each groove is blazed at an angle Θ_B with respect to the normal (dashed line). The incidence angle is marked α and β is the angle of diffraction.

blaze angles for echelle gratings are 63.4° and 75.9° . The tangent of 63.4° is 2 and grating with this angle is called "R2 grating", a tangent of 75.9° is 4 and therefore named "R4 grating".

For a constant diffraction angle $\beta = \beta_c$ the grating equation 1.21 has the following form

$$\lambda_c(m) = \frac{d}{m}(\sin \alpha + \sin \beta_c), \quad (1.25)$$

where λ_c is the central wavelength of an order. Derivation of the relation with respect to m we obtain $d\lambda/dm \sim 1/m^2$. This implies that the distances between the central wavelengths will decrease as $1/m^2$ and at high orders the wavelength intervals will overlap. To be able to record separated spectral orders at the same time cross-dispenser is used.

Echelle grating is designed to have maximum efficiency in a given diffraction order. Thus, the maximum optical power is in the preferred diffraction order and power in the other orders is minimized. This can be achieved only for one specific wavelength. The maximum efficiency in a particular order is achieved with blaze angle Θ_B (Hatzes, 2019).

1.3.1 Ondřejov Echelle Spectrograph (OES)

The first steps to build an echelle spectrograph in Ondřejov were made by P. Koubsky and his team in 2000 (Koubský et al., 2004). In 2007, the OES was fully operating. It is installed on the Ondřejov Perek 2-m telescope and designed as a white-pupil spectrograph (Kabáth et al., 2020). Originally, OES was built as a slit spectrograph, but after modernization in 2019, it is a fibre-fed high-resolution

spectrograph. In the original configuration of the telescope, there were 6 optical surfaces in total, including 4 mirrors and one glass plate, before reaching the Coudé focus. Each mirror represents a light loss which increases exponentially with the number of surfaces. The modernization consisted of the replacement of this optical path with optical fibre (Šlechta, 2020).

The optical design is shown in Figure 1.6. The light reflected from the main mirror is directed via optical fibre from the primary focus to the coudé room where it is reflected to a Zerodur echelle grating. Echelle grating was made by Richardson Grating Laboratories. It has blaze angle $\Theta_B = 69^\circ$, size 157×412 mm and 54.5 grooves/mm. The light is then reflected by an optical mirror to an equilateral prism, made by TOPTEC Turnov. The prism separates the orders that are then brought to a focus on the detector. The detector is a CCD Camera Versarray 2048B (Roper Scientific) it is cooled with nitrogen to its working temperature -110°C . For the calibration, a Th-Ar lamp is used. Iodine cell is also possible to use. The wavelength coverage of OES is $3753 - 9195 \text{ \AA}$. The resolving power $R = 51600$ at 5000 \AA and spectral sampling is 2.4 \AA/mm . The number of orders that can be extracted is 56 [E03].

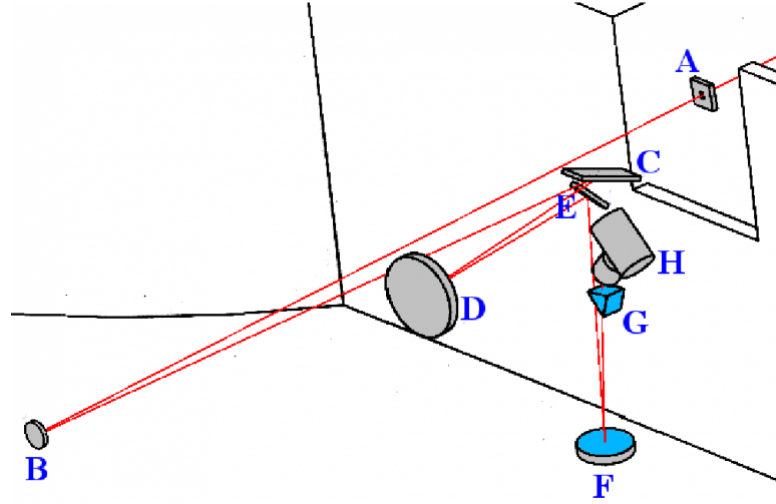


Figure 1.6: Optical layout of OES [E03]. The path of the light is from the Coudé room through the slit A to collimator B. From there the light travels to an echelle grating C and then to a first parabolic mirror D and a small flat mirror E. F is a second parabolic mirror from this mirror light goes to prism G and it ends at objective lens and dewar vessel H.

1.4 Sources of radial velocity measurement errors

The precision of the RV measurements depends on several aspects. The overall performance of the spectrograph and its instrumental errors, observing strategy, wavelength calibration method, the star's properties and stellar variability. Wavelength calibration has a major effect on accuracy of RV measurements and will be described in bigger detail in Section 2.2.

1.4.1 Influence of the instrument and the data properties

Characteristics of a spectrograph such as a wavelength coverage and resolving power and data properties like the signal to noise ratio (SNR) can influence the precision.

The resolving power R plays a role when recording the width of the spectral line and how easy it is to detect the centroid of the line. It describes how many spectral elements $\delta\lambda$ it is possible to resolve at a given wavelength

$$R = \frac{\lambda}{\delta\lambda}, \quad (1.26)$$

where $\delta\lambda$ is the spectral resolution defined as the difference in wavelength of two monochromatic beams that can just be resolved by the spectrograph. Spectral resolution $\delta\lambda$ has a dimension of length and the smaller it is the easier it is to recognize spectral details. Resolving power R is a dimensionless quantity and the larger it is the higher the resolution.

SNR mostly depends on the brightness of the star, the exposure time and the observing conditions but when these aspects are constant then the only thing that affects SNR is the efficiency of the telescope, spectrograph and detector.

The larger the wavelength coverage of the spectrograph, the more spectral lines that can be used for the measurements of the Doppler shift we have. Measurements of a Doppler shift from every spectral line have a certain error. If we use more lines, the measurement uncertainty decreases by a factor of \sqrt{N} , where N is the number of used spectral lines. In other words, the expected RV error on some wavelength range $\Delta\lambda$ is (Hatzes, 2019):

$$\sigma_{\text{RV}} \propto (\Delta\lambda)^{-0.5}. \quad (1.27)$$

This relation is only theoretical and in reality, it is more complicated. First, when the wavelength coverage is increased it does not always end up in a large number of useful lines for Doppler measurements. It depends on the effective temperature of the star because in some spectral regions the density of the spectral lines is smaller. And also not all spectral lines have the same intensity. The next problem is when wavelength coverage is extended beyond $\approx 6000 \text{ \AA}$. In this region, telluric lines start to be prominent. These lines are not tied to the Doppler motion of the star because they are caused by the oxygen and water vapour in our atmosphere, but they can be used to decrease the RV error.

The error in the data σ_p is determined only by number of detected photons N_p when there is no other source of noise. According to photon statistics, $\sigma_p = \sqrt{N_p}$.

The limit to the RV precision that is possible to achieve for a given exposure is given by photon noise. RV error is (Hatzes, 2019):

$$\sigma_{RV} \propto (\text{SNR})^{-1}. \quad (1.28)$$

Increasing the SNR lowers the RV error. With a given instrument and telescope, to increase the SNR the exposure time has to be increased. It is possible, but it is inefficient because exposure time can not go to infinity. Firstly, the longer the exposure time, the more cosmic particles hit the CCD, and secondly, the systematics errors and intrinsic stellar variability will set the precision of the RV before the photon noise limit is reached. Thus, not an effective use of the telescope time.

RV precision is also affected by the spectral resolution $\delta\lambda$ of the spectrograph. The Nyquist criterion, which says that two detector pixels cover the spectral resolution, is satisfied for the most spectrographs designs. Several studies were made to find how the RV uncertainty depends on resolving power R . It follows a power-law (Hatzes, 2019)

$$\sigma_{RV} \propto R^{-\alpha}, \quad (1.29)$$

where $\alpha = 1 - 1.5$. A good approximation is to use $\alpha = 1.2$. The highest resolving power possible is not the best solution for better RV precision. Firstly, a high-resolution spectrograph means that every part of the spectrograph is larger, which means more expensive. Secondly, the dispersion of the light at high resolving powers is higher, which results in a decrease of count rate and SNR.

1.4.2 Influence of the stellar characteristics

Stellar characteristics also influence RV precision. The main three are the projected rotational velocity $v \sin i$, the strength of stellar spectral lines and the number density of stellar lines.

The rotation of the star makes the spectral lines wider and shallower, which makes it more difficult to find the centroid. This characteristic makes early-type stars worse targets for Doppler measurements.

The RV uncertainty due to the stellar rotation is (Hatzes, 2019):

$$\sigma_{RV} \propto (v \sin i)^\beta, \quad (1.30)$$

where $\beta = 0.2$ for $v \sin i < 2 \text{ km} \cdot \text{s}^{-1}$ and $\beta = 1.3$ for $v \sin i > 10 \text{ km} \cdot \text{s}^{-1}$.

Spectral line strength needs to be also, taken into account. Weak lines get lost in the noise. The depth of the line does not scale linearly with the line strength. The line depth increases, and the width remains quite constant when the line begins to saturate, the depth of the line no longer increases, but the line width grows. This property implies that lines best for the RV measurements are strong but not yet saturated.

A number of spectral lines depend on the effective temperature of the star. For example, early-type stars are hot and the number density of stellar lines is low. For $T_{\text{eff}} < 5000K$ the scaling actor for the RV error is (Hatzes, 2019):

$$F = 0.16e^{1.79(T_{\text{eff}}/5000)}. \quad (1.31)$$

1.4.3 Overall formula for the uncertainty

After putting all influences described above together, we obtain a grand scaling relationship for the expected RV precision. It includes SNR, resolving power R , effective temperature T_{eff} and projected stellar rotational velocity V (Hatzes, 2019).

$$\sigma[\text{m} \cdot \text{s}^{-1}] \propto \Delta\lambda^{-0.5} (\text{SNR})^{-1} R^{-1.2} f(V) (0.16e^{1.79(T_{\text{eff}}/5000)}) \quad (1.32)$$

where the $f(V)$ is the function of the projected rotational velocity

$$f(V) \propto 0.62 + (0.21 \log R - 0.86)V + (0.00260 \log R - 0.0103)V^2. \quad (1.33)$$

From the equation, 1.32 follows that for precise measurements instrument with high resolving power R and wide wavelength range $\Delta\lambda$ is needed. This is why echelle spectrographs are used. Echelle spectrography is described in Section 1.3.

Methods to calculate Doppler shifts

There are two methods how to calculate Doppler shifts. The iodine cell method is the main topic of my thesis, but I also used the cross-correlation method on my data set to see the difference in the results. For iodine cell method, I was using `viper` (Zechmeister et al., 2021) and IRAF (Image Reduction and Analysis Facility, Tody, 1986) was used for cross-correlation method. IRAF is also used for extraction and further reduction of the observed data.

2.1 Basic data reduction with IRAF

Data from OES are in the FITS format and for their extraction and further reduction, IRAF is used. IRAF is software created at the National Optical Astronomy Observatory (NOAO). It was created for the reduction of raw astronomical images. As the reduction of the spectra was not the purpose of my work I will not go into much detail and describe it only briefly.

The first step before any scientific process is correcting the image because not every part of the echellogram is usable. There can be some bad pixels or blurred edges mainly because the optical path has its imperfections. For bad pixels, it is possible to use a bad pixel mask which does linear interpolation along lines or columns using the nearest good pixel. Bad pixel regions have to be defined by the user. Task "fixpix" in IRAF is used for this. Another problem is caused by cosmic particles, they hit the CCD and leave unwanted marks on the image. The number of particles is related to the length of exposure and also Sun activity. For removing cosmic particles, task "cosmicrays" is used. Blurred edges can be simply removed by trimming the frames. The echellogram takes up only a part of the frame, thus parts of the image without the echellogram are removed too. For this, task "imcopy" is used. An example of raw data is in Figure 2.1a and the image after bad pixel and cosmic particles removal and cropping of redundant parts is in Figure 2.1b.

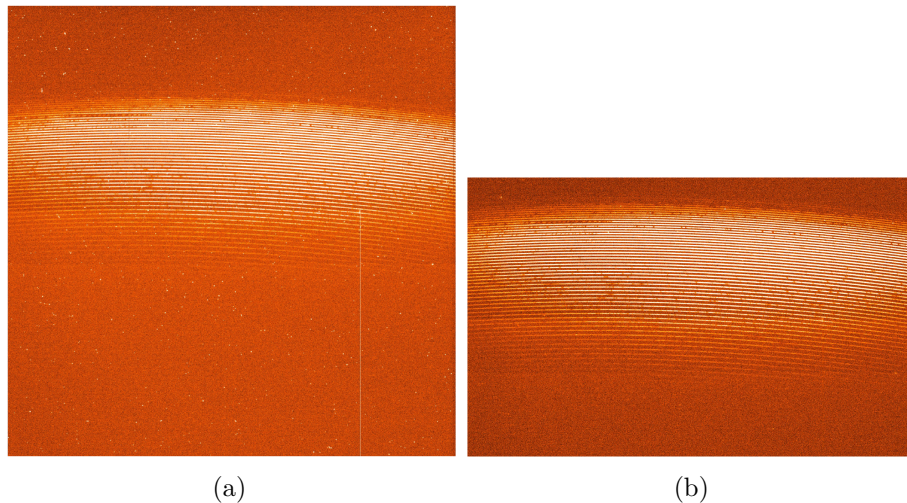


Figure 2.1: Example of data from the OES: (a) Raw image, (b) Image after bad pixel and cosmic particles removal and cropping redundant parts of the image.

The second step is subtracting the master bias and creating a master flat. Bias frames are used for removing the readout noise. Flat frames are used for correcting the variations in the illumination of the chip and pixel-to-pixel sensitivity. There are several bias frames taken and then combined into master bias and the same with flat frames. The combination of the frames into one master frame is done by task "imcombine".

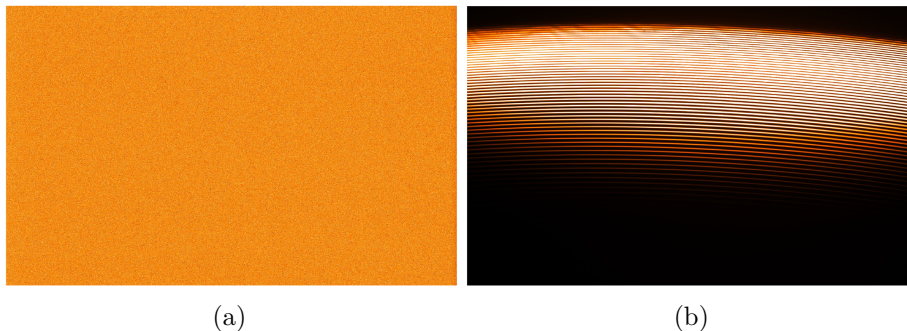


Figure 2.2: (a) Bias frame, (b) Master flat frame

The next step is aperture extraction. The light from the spectrograph is divided into apertures (orders). Every aperture has a differently curved shape and for tracing the shape, the task "apall" is used. First, a template for the extraction of apertures is made. For this, apertures are made usually on A-type stars such as Vega that have defined apertures in the blue region of the spectrum. This template is used for extracting the apertures from all the scientific frames, master flat and also Th-Ar frame. Echellogram of Vega is shown in Figure 2.3.

The uneven illumination of the apertures can be corrected with the normalised



Figure 2.3: Echellogram of Vega.

flat frame which is made using ask "apflatten". Then all the scientific frames and ThAr frame can be divided by the normalised flat frame using the task "imarith". After this, light from the apertures can be extracted and two-dimensional spectra as a function of pixels are obtained. This spectrum needs to be calibrated to wavelengths.

For the wavelength calibration, a Th-Ar emission lamp is used. A comparison spectrum of Th-Ar with emission lines at known wavelengths is taken. Lines in this spectrum need to be identified and the relation between pixel and wavelength is determined using the task "ecidentify". Subsequently, pixels are converted to wavelength in all spectra using task "dispcor". An example of the flux non-normalised 2-d spectrum in one of the apertures is shown in Figure 2.4.

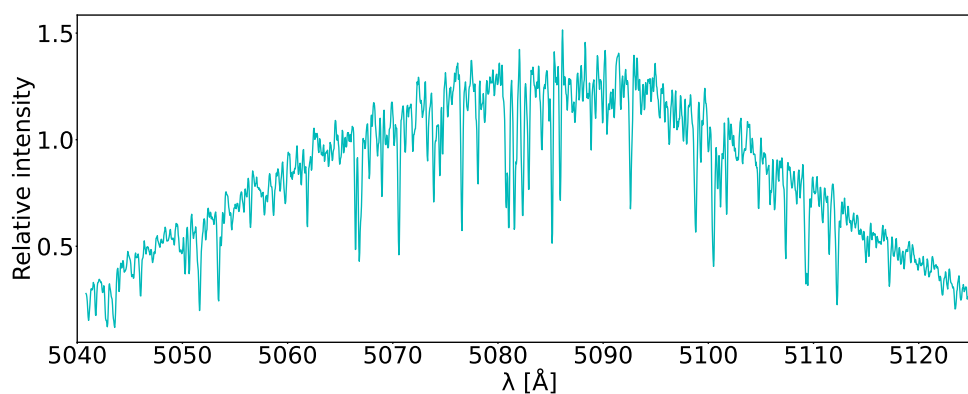


Figure 2.4: Example of non-normalised 2-d spectrum (only aperture 19 shown).

The following step is flux normalization. It is done by using the task "continuum". An example of normalised 2-d spectra is shown in Figure 2.5. It is also possible to merge all the orders into a one-dimensional spectrum. It is done in four steps, firstly normalization function is calculated using task "sarith", secondly non-normalized spectra are merged, and then normalization functions are also merged using task "scombine". The last step is dividing merged non-normalized spectra by merged normalization functions (task "sarith"). An example of a 1-d merged spectrum is shown in Figure 2.6.

In the red part of the spectrum, orders do not overlap and drops in intensity occur there. It can be solved by replacing zero values with value one.

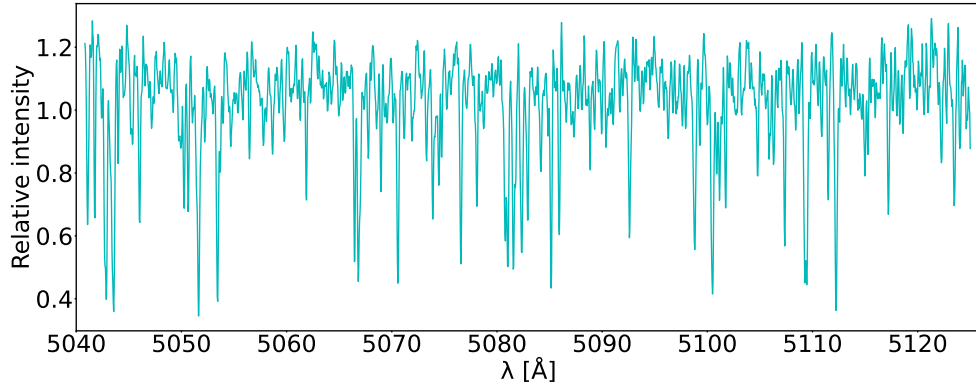


Figure 2.5: Example of 2d normalised spectrum (only aperture 19 shown).

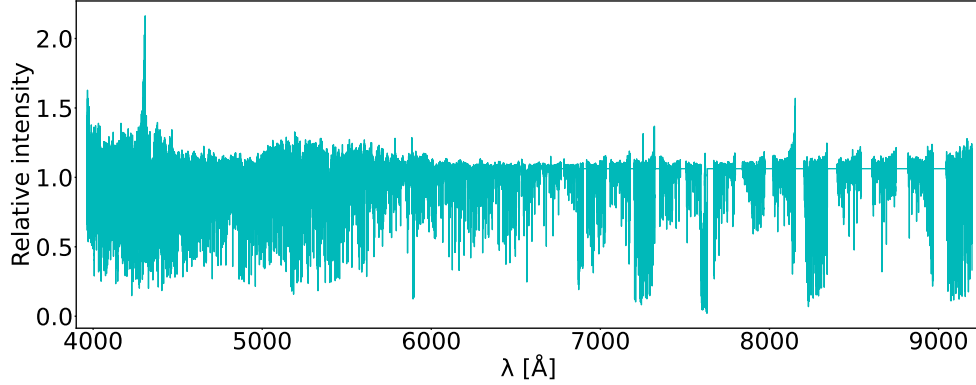


Figure 2.6: Example of 1d normalised spectra

2.2 Wavelength calibration and RV determination

The shift of the absorption lines in stellar spectrum is recorded on the CCD detector in pixels. With wavelength calibration we can convert pixels to wavelengths. There are several methods for this, Hollow cathode lamps, Telluric method, Gas cells, Laser frequency combs and Fabry-Pérot etalons.

Hollow cathode lamps

Hollow cathode lamps, also called emission lamps, are used for reference wavelength spectrum. Most commonly used are thorium-argon (Th-Ar) or uranium-neon (U-Ne) lamps. Reference spectrum can be taken simultaneously with observations or before/after the observations. The precision of the measurement is much higher if the reference spectrum is taken simultaneously because it is taken with the same conditions as a spectrum of the star. Th-Ar lamp is used because it has strong emission lines over a wide optical to infrared range. U-Ne lamps have higher line density in the near-infrared and the problem with very bright noble gas lines is less prominent. One of the disadvantages of emission lamps is a significant ageing effect. This can be solved by installing two lamps, one used for every observation and the other one used as a calibrator only rarely (Perryman, 2018). This method was used for the discovery of 51 Pegasi using ELODIE spectrograph (Mayor and Queloz, 1995). It was achieved with the reference spectrum taken simultaneously with the observations. Th-Ar lamp is also used for OES wavelength calibration, but the reference spectrum is taken after the exposure.

Telluric method

The telluric method is using water vapour and oxygen lines that imprint in the stellar spectrum while passing the Earth's atmosphere. This method solves the problem of the light going through different optical paths of the light from the star and emission lamp. The disadvantage is the limited spectral range of the telluric lines and also the instabilities in our atmosphere, like different path length depending on the position on the sky. Also, wind can affect the observations with a systematic shift up to $20 \text{ m} \cdot \text{s}^{-1}$. Short- and long-term stability analysis was made with HARPS. Archival data over 6 years were used. The stability check of the telluric lines was performed on τ Cet, μ Ara and ϵ Eri, with the HARPS instrument. It was found that the long-term stability of telluric lines is $\sim 10 \text{ m} \cdot \text{s}^{-1}$ and short-term $\sim 2 \text{ m} \cdot \text{s}^{-1}$ (Perryman, 2018).

Gas cells

The gas cell method is using gas cell which is in the path of the incoming light. The principle of this method is the same as for telluric lines, but the stability of the lines is higher and the wavelength range is wider for the cell method. Then absorption lines of known wavelengths are imprinted into the stellar

spectrum. This provides a wavelength calibration and also information about the instrumental profile can be obtained. One of the first gas cells were filled with hydrogen fluoride (HF) which is good for its well-spaced line distribution but it is also toxic and corrosive. Currently, the more commonly used gas is iodine (I_2). It has a large number of strong absorption lines. The disadvantage of iodine is that the wavelength range is $\sim 5000\text{-}6000 \text{ \AA}$, which is not ideal for M dwarfs (Perryman, 2018). The iodine cell method is the method I used for this thesis and I tested it for use at OES, thus it is described in bigger detail in Section 2.4.

Laser frequency combs

Laser frequency combs provide a reference spectra that covers the entire optical and IR range with individually unresolved lines with uniform spacing and intensity. With this method, it is possible to achieve detection of exoplanets at $\sim 0.01 \text{ m} \cdot \text{s}^{-1}$ level. This method is based on the femtosecond (fs) mode-locked laser which provides pulses with a repetition rate, T , and a pulse duration, τ , of fs. Using Fourier transform repetition rate and pulse duration are transformed into a frequency domain. The comb has repetition frequency T^{-1} and the spectral width of the comb τ^{-1} is \sim several hundreds terahertz. The pulse rate is synchronized with an atomic clock. One of the problems of this method is that there are too many peaks for wavelength calibration. There are so many peaks that in a typical high-resolution spectrograph they blend together. Fabry-Pérot filter needs to be added to reduce the number of peaks (Hatzes, 2019).

Fabry-Pérot étalons

Fabry-Pérot étalons or interferometers provide quasi-periodic and dense lines with homogeneous amplitudes. It is a more economical alternative to Laser frequency combs. F-P interferometer consists of two plane-parallel surfaces with high reflectivity separated by a distance. One part of the beam is transmitted and the other is reflected between the two plates (Hatzes, 2019).

2.3 Cross-correlation method

One of the methods how to determine Doppler shift is the so-called cross-correlation method. The mathematical relation is (Hatzes, 2019):

$$\text{CCF}(\Delta x) = s(\Delta x) \otimes t(\Delta x) = \sum_{x=1}^N s(x)t(x + \Delta x)dx, \quad (2.1)$$

where $s(x)$ is stellar spectrum as a function of pixels and $t(x)$ is a template spectrum, CCF is cross-correlation function and Δx is the lag of the CCF.

The CCF is most sensitive to Δx when s and t are the same because CCF is a measure of the similarity of two signals. In IRAF it is done with task "fxcor".

For good results with this method is important to have a high SNR template that is similar to the spectrum of the target star. The resulting RVs are relative to the template.

Before the CCF telluric correction is done, atmospheric lines are used for removing the instrumental influence. It is done with task "fxcor". Cross-correlation of the region of telluric lines is done. For results in Section 3.7 I used telluric lines in the interval 6865 - 6895 Å. Heliocentric correction also needs to be done, it is a procedure where the doppler shift caused by Earth's motion around the Sun and Earth's rotation is removed. For this task "rvcorrect" is used. Barycentric correction, which removes the influence of the Earth's motion around the barycentre, can be done too. This influence is only in the order of units $\text{m} \cdot \text{s}^{-1}$, therefore I did not do it for my results in Section 3.7. The final shift of the spectrum by the value of telluric and heliocentric correction is done with task "dopcor".

2.4 Iodine cell method

The iodine cell method is already shortly described in Section 2.2. It is also possible to use the cross-correlation method with iodine cell but the main advantage of the iodine cell method is that it gives us a piece of information about the instrumental response. Other advantages are temperature and pressure stability and overall long-term stability, accuracy up to units $\text{m} \cdot \text{s}^{-1}$. Also, the typical length of the cell is 4-15 cm making the cell compact and easy to use. Disadvantages are wavelength range, spectrum contamination and light loss. Spectrum contamination is making it more difficult to use iodine cell observations for further analyses, like abundance studies, stellar parameters measurements and spectral line shapes examination. The loss of light is between 20-50 %, depending on the amount of iodine in the cell.

Three main components for determining RVs with the iodine cell are:

1. A fiducial which is a high-resolution spectrum of iodine taken with the cell.
2. A template which is a high-resolution spectrum of the star taken without the iodine cell.
3. A spectrum of the star taken with the cell.

Figure 2.7 shows aperture 20 of the σ Draconis spectrum (observation template), the corresponding part of the spectrum of iodine (FTS) and the spectrum of the σ Draconis with the iodine spectrum (observation).

The fiducial is made after the construction of the iodine cell, and it is scanned using Fourier Transform Spectrometer (FTS). It should be done at the highest resolving power possible, at least $R = 500\,000$. Fiducial can be also made using a spectrograph used for the observations, however, this lowers the precision of the radial velocity by a few $\text{m} \cdot \text{s}^{-1}$ (Hatzes, 2019)

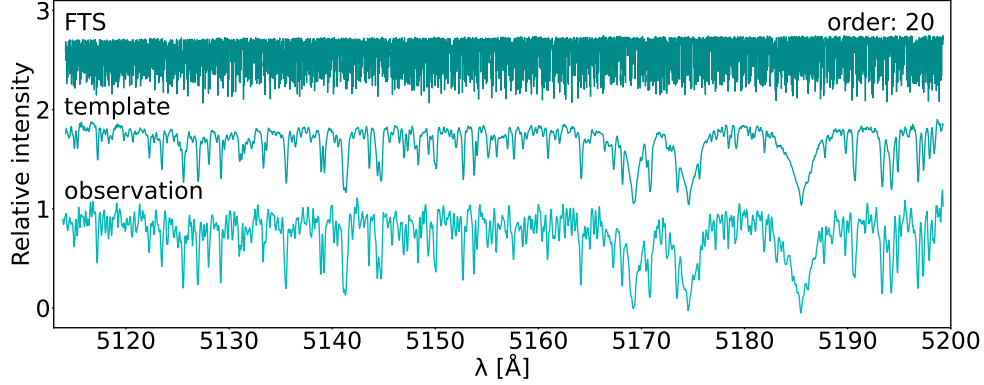


Figure 2.7: Spectra of aperture 20 of iodine cell (FTS), σ Draconis template and σ Draconis observation.

It is possible to make the template as a spectrum of a star without the iodine cell. This spectrum should have as high signal to noise ratio (SNR) as possible. There is one difficulty when taking the template with a spectrograph used for the observation because there is an instrumental profile (IP) included in this spectrum. And when calculating the radial velocities we convolve the template with IP so we need to use the deconvolved stellar spectrum for the highest precision of RVs. There is no problem with using a template containing IP at the cost of lower precision.

RVs are calculated via solving the equation (Butler et al., 1996):

$$I_m = k[T_{I_2}(\lambda)I_S(\lambda + \delta\lambda)] * IP, \quad (2.2)$$

where I_m is the model spectrum, I_S is the intrinsic (deconvolved) stellar spectrum (template), T_{I_2} is the transmission function of the iodine cell (FTS), k is a normalization factor, $\delta\lambda$ is the wavelength (Doppler) shift, IP is the instrumental profile and $*$ represents the convolution.

2.4.1 Instrumental Profile (IP)

The instrumental response of a spectrograph is described with the IP. An explanation of this is illustrated in Figure 2.8. If the spectrograph would be perfect, e.i. no influence of the optical path on the light, then when monochromatic light with an infinitesimally small width in wavelength (δ function) would pass through this instrument there would be no change in this light. Real spectrographs do not work like this and when δ function is passing through, we get a blurred function, typically with a Gaussian-like profile. In case of δ function the resulting function is IP.

When observing a stellar spectrum, the whole spectrum is convolved with IP, if the IP is asymmetric then this asymmetry will be included in the spectrum. When measuring RVs we do not care about the shape of the IP because we are

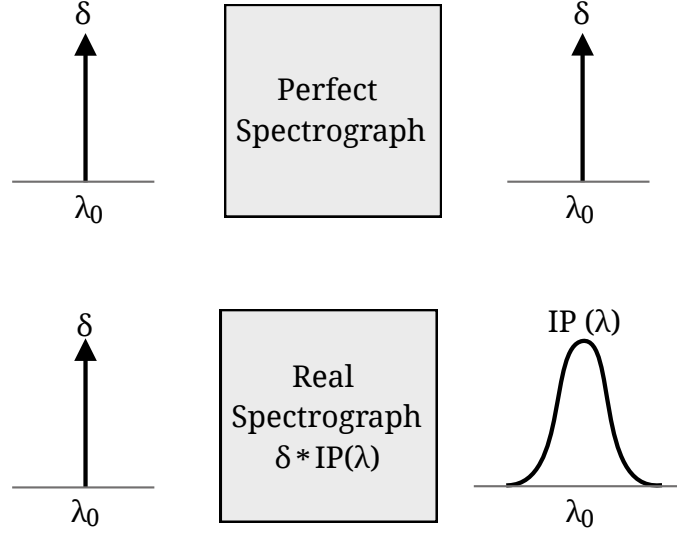


Figure 2.8: Illustration of the IP function. A perfect spectrograph with no instrumental response (top panel). For a real spectrograph with an instrumental function (bottom panel). Based on Hatzes (2019).

measuring relative doppler shifts. The only problem is when the shape of the IP is changing in every observation we make. In Figure 2.9, two situations are illustrated. On the left, there is an asymmetric IP with the centre of the line shifted by $+0.17$ pixels from the centre of a symmetric IP. This shift introduces a change in velocity of $250 \text{ m} \cdot \text{s}^{-1}$. This would not be a problem if this shift would be the same in all observations because it would only mean an offset of $250 \text{ m} \cdot \text{s}^{-1}$ for all data points. The problem arises when there would be center of the line shifted by -0.17 pixels ($\Delta v = -250 \text{ m} \cdot \text{s}^{-1}$) in the second observation. This would mean a change in RVs of $+500 \text{ m} \cdot \text{s}^{-1}$ from the first observation. This change in RVs is not from the star and it is only a change in the shape of IP.

Unless the spectrograph is mechanically and thermally stable, placed in a vacuum tank at low pressure, there will always be a change in IP in every observation and it will result in an instrumental Doppler shift. Building a stable and very precise spectrograph is expensive. However, we can get very precise RV measurements also with a common spectrograph. The solution is in the usage of the iodine cell.

It is possible to use the information about the IP from iodine lines and model the IP. The idea of modelling the IP was proposed by Valenti et al. (1995). They proposed taking a very high-resolution spectrum of iodine with FTS and then rebin it to the same resolution as the spectrograph that is used for observation. The result of this is a good representation of the response of the spectrograph and from this, it is possible to find a model for the IP. The product of this model

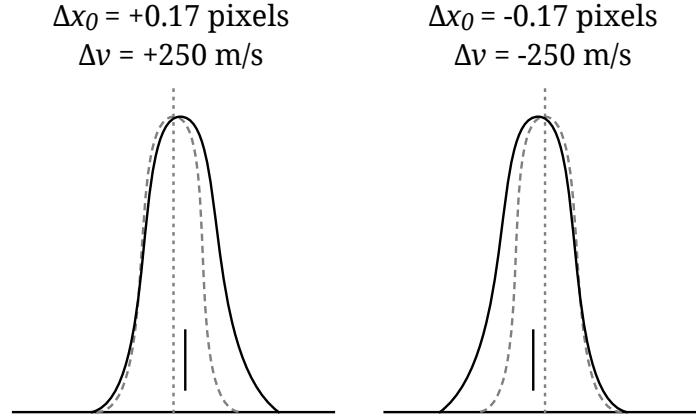


Figure 2.9: The solid line is an asymmetric IP. The dashed line is symmetrical IP. The vertical line represents the centroid of the asymmetric IP. Based on Hatzes (2019).

for the IP convolved with the original FTS is the observed iodine spectrum.

The majority of the pipelines used for iodine cell data reduction are using the method first described by Valenti et al. (1995). This method is based on modelling the IP as a sum of Gaussian functions. IP in its principle is a Gaussian profile and the additional satellite Gaussian components make it easy to reproduce the asymmetries.

CHAPTER 3

Setting up viper for OES data

For purpose of this thesis, I was using already reduced spectra taken with OES by observers from the Stellar Department of the Astronomical Institute of the Academy of Sciences of the Czech Republic in Ondřejov. The stars used for my testing were HD 10780, HD 182572, σ Draconis (RV-null standard stars), HD 187878 (red giant star observed as a part of the Ondřejov program) and 51 Pegasi (well-studied exoplanet). Parameters of these stars are listed in Table 3.1.

Table 3.1: Basic parameters of stars used for analysis.

ID	α [°]	δ [°]	Sp. type	V [mag]	RV [km/s]
σ Draconis	293.10	69.65	K0 V	4.68	26.734
HD 10780	26.94	63.85	K0 V	5.63	2.840
HD 182572	291.25	11.95	G8 IV	5.16	-100.212
HD 187878	297.61	43.66	K0 E	7.13	-18.58
51 Pegasi	344.37	20.77	G2 IV	5.46	-33.165

* Values obtained from SIMBAD [E04].

3.1 Introduction to viper: Velocity an IP Estimator

The main task of my thesis was to work with data from the OES and use `viper` to calculate radial velocities. `viper` is a Python-based software currently being developed. It processes stellar spectra taken using iodine or other gas cells and measures radial velocities. It is based on work by Butler et al. (1996). It convolves the product of a stellar template and a gas cell spectrum with an instrumental profile. Then it optimizes the parameters of the instrumental profile, the wavelength solution, flux normalization, and the stellar Doppler shift using least square fitting. It also offers different functions to describe the instrumental profile, e.i. Gaussian, super-Gaussian (it is an extension of the Gaussian which allows to represent a variety of different shapes by adding just one free shape parameter), skewed Gaussian or mixtures of Gaussians. `viper` code works with echelle spectra and it can process data from CES, CRIRES+, KECK,

OES, TCES, and UVES, and new instruments can simply be added. **viper** can be found at <https://github.com/mzechmeister/viper>. The Graphic User Interface is shown in Figure 3.1.

Basic steps how **viper** works are:

1. bad pixel/data removal
2. telluric lines downweighting or removal
3. barycentric correction
4. stellar template is multiplied with the FTS and convolved with IP according to the equation 2.2
5. least-square fitting to optimize RV, IP, wavelength solution, normalization
6. create the model for the best fit of observed spectra
7. gives the relative RV in respect to the stellar template

Several parameters can be set. First, data files and template paths are given. Input data for **viper** are wavelength calibrated spectra, it can be 2 dimensional or 1 dimensional, normalised or non-normalised. These spectra are obtained after data reduction of the echellogram. 2d spectrum is a spectrum divided into apertures, 1d spectrum is a spectrum where all apertures are put together. Examples of these spectra are in Section 2.1. Then telescope is chosen, for Ondřejov data option OES. Targ parameter is optional but it is needed for OES. This parameter is the name of the target as used in SIMBAD (Wenger et al., 2000), it collects coordinates (right ascension (RA), declinationlonger (DEC)), proper motion, parallax and absolute RV of the star. The parameter tag is for

The screenshot shows the graphical user interface of the **viper** software. It is divided into several sections:

- data files**: Includes a "Search data file" button and a text input field containing "data/OES/*.fits*". Below this is a "telescope:" dropdown menu set to "OES" and a "targ:" text input field.
- template file**: Includes a "Search tpl file" button and a text input field containing "data/OES/*.fits". Below this is a "tag:" text input field.
- Options data reduction**: A section with various parameters:
 - nset: [:]
 - oset: [20:27.28]
 - chunks: [1]
 - kapsig: [4.5]
 - oversamp: [1]
 - stepRV: []
 - IP: [g]
 - iphs: [70]
 - vguess: [1]
 - dega: [8]
 - degb: [3]
 - degc: [1]
- Options plotting data**: A section with checkboxes for:
 - raw data
 - plot IP
 - stellar tpl
 - forward model
 - lookres
 - fit continuum
 - wavelength solution
 - fit vguess
 - lookguess
 - lookpar
- Buttons**: "Start" and "EXIT" buttons are located at the bottom right.

Figure 3.1: The Graphic User Interface of **viper**. Parameters used for OES data are shown.

the output file name, it is an optional parameter and by default, output files are named by "tmp".

The second part of the GUI is "Options data reduction". Parameter "nset" is used for choosing which or how many data files will be processed. Parameter "oset" is used for choosing which apertures of the spectra will be used. For a better result, choose only "good" apertures. Parameter "chunks" is for dividing spectra into several chunks. For processing one aperture as a whole 1 is set. Parameter "kapsig" is for the flag or clip the bad data over a given value and removes outliers. It is important not to use too small number. Another parameter "oversampling" is used for oversampling template data by a given value. Value 1 is a cubic spline. Next is "stepRV", this parameter is not needed for calculating good RVs, but it helps to find and understand problems in data reduction. It steps through fixed RVs to find the minimum in the rms, there are two options, m: (manual) uses a fixed range and steps around vguess, a: (auto) picks the fixed RVs automatically to get close to the minimum. Next is "IP", which selects the shape of the IP (g: simple Gaussian, ag: asymmetric (skewed) Gaussian, sg: super-Gaussian, mg: multiple Gaussians (two), bnd: bandmatrix). Another parameter is "iphs". It is used for determining the width of the Gaussian, it is important to check if it is not too small. Parameter "vguess" is a starting point for RV guess in $\text{km} \cdot \text{s}^{-1}$. Parameter "dega" is a degree of a polynom for normalisation. Parameter "degb" is the degree of the polynom for wavelength solution. Parameter "degc" is a degree for cell offset, it can be 0 or 1. Initial guess of parameters values were kindly provided by Jana Köhler. Parameters found as the best for the OES data are shown in Table 3.2. The analysis has shown that, the best apertures that can be used for OES data are 20-28 without 27 (parameter "oset"). It is shown in a bigger detail in Section 3.3. Other parameters were selected based on testing (shown in Section 3.2). A window that appears after pressing start is shown in Figure 3.2.

Table 3.2: The best found parameters for OES data.

Parameter	value
oset	20:27,28
chunks	1
kapsig	4.5
oversampling	1
IP	g
iphs	70
vguess	1
dega	8
degb	3
degc	1

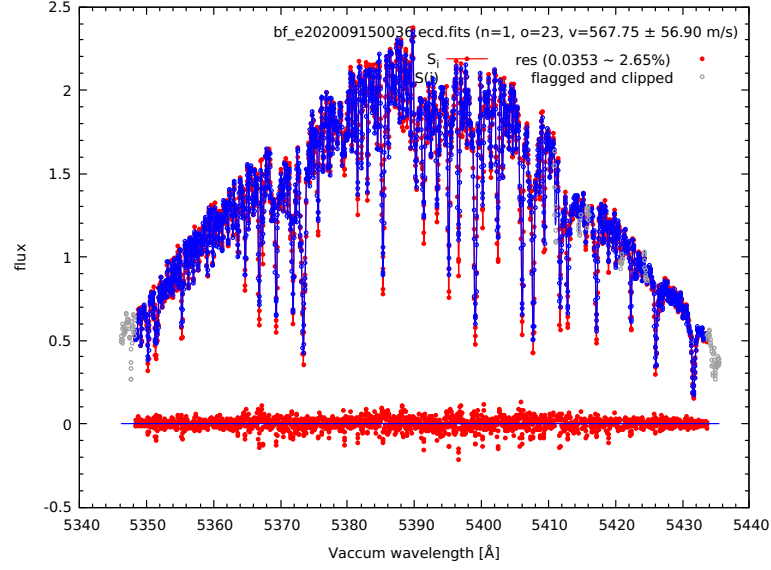


Figure 3.2: **viper** window with observed spectra (red), modeled spectra (blue), clipped/flagged data (grey) and residuals (observation - model) (bottom).

The final part of the GUI is "Options plotting data". This part is not important for data processing, but useful for the study of the data and modelling and identifying problems in data and modelling. Option "raw data" plots raw data, model and iodine cell. "Plot IP" plots the initial guess of the IP. "Stellar tpl" plots template (model*IP). "Forward model" plots model results with fixed starting values. "Lookres" gives a closer look at the residuals. "Fit continuum" fit model with variable normalization. "Wavelength solution" fit model with variable wavelength solution. "Fit vguess" fit model with variable normalization, wavelength solution. "Lookguess" shows the initial model. "Lookpar" shows results and errors of fitted parameters.

3.2 Testing of parameters

I tried several combinations of the input parameters. A useful tool for testing input values is "lookpar". The window of "lookpar" is shown in Figure 3.3. There are three plots in this Figure, the top left panel shows the continuum fit, the top right panel shows the wavelength solution fit, and the bottom left panel shows the IP fit. These plots were obtained when parameters listed in Table 3.2 were used. It is the best result that can be obtained, but it is not perfect. An example of much better performance of **viper** is shown in Figure 3.4. These plots were obtained using data from Thüringer Landessternwarte Tautenburg (TLS). For **viper** it is much easier to fit data from TLS because TLS has a better design and spectra have good quality. Furthermore, the IP of the TLS is much more stable.

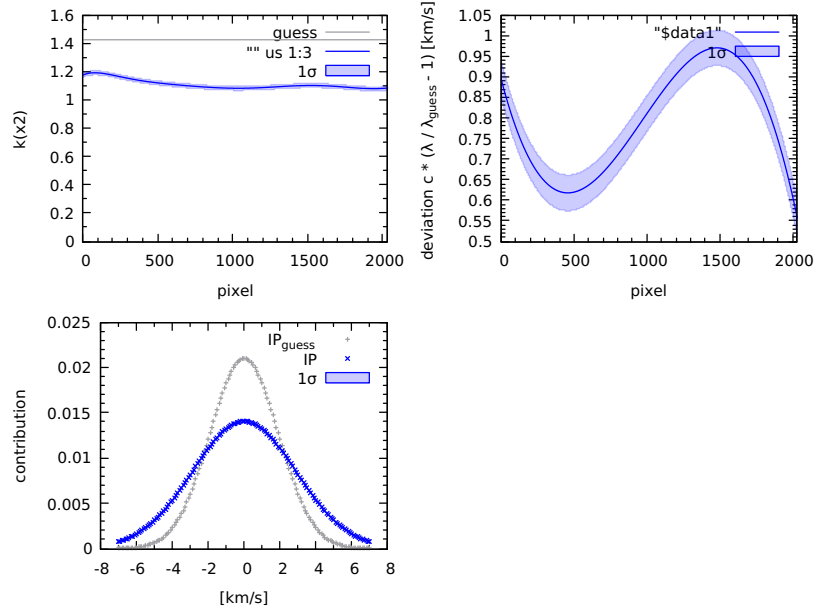


Figure 3.3: A window of "lookpar" option for OES data. A plot of the continuum fit (top left panel), a plot of the wavelength solution fit (top right panel) and a plot of the IP fit (bottom left panel).

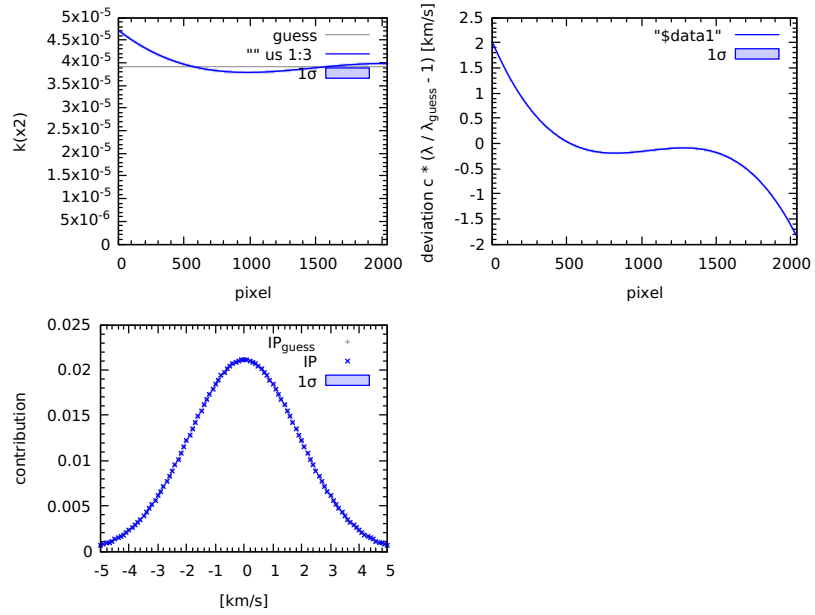


Figure 3.4: A window of "lookpar" option for TLS data. A plot of the continuum fit (top left panel), a plot of the wavelength solution fit (top right panel) and a plot of the IP fit (bottom left panel).

Parameter "dega" is a degree of a polynom for normalization, if it is too low the continuum is not fitted well, and when too high there are too many parameters to solve, and computational time gets longer and there is no significant improvement.

The degree of the polynom for wavelength solution is parameter "degb". As can be seen in Figure 3.3 wavelength solution is hard to model for *viper*. If a value higher than 3 is used *viper* fails to model wavelength solution. It is caused by the FTS quality.

The third plot in Figure 3.3 is related to IP. It can be affected by changing the IP shape (parameter "IP") and the IP width (parameter "iphs"). Using simple Gaussian (option "g") as a shape of the IP gives the best results. In terms of IP width, choosing a value around 70 - 90 was giving similar results.

While testing, the default values of other parameters turned out to be the most suitable to get the best results.

3.3 Which apertures to use?

One of the disadvantages of using the iodine cell method is that lines of iodine are only between 5000 - 6000 Å. Thus, the first step in OES data analysis was to find out which apertures of the spectrum are in this interval. This wavelength interval corresponds to apertures from 19 to 30. Examples of these apertures are shown in Appendix A. In Figure 3.5 RVs for σ Draconis in individual apertures are plotted. σ Draconis is a main-sequence star.

From Figure 3.5, it can be seen that apertures 19, 27, 29 and 30 have significantly worse results than other apertures. This problem occurs for all of my target stars and the reason is the FTS. In apertures 19, 29 and 30 (Figures A.1, A.11, A.12) are too few iodine lines and in aperture 27 there is the opposite problem, there are too many lines and they blend with the lines of the star. Due to this, there is a significant decrease in the continuum around 5720 Å (Figure A.9). Based on this, we decided to exclude these apertures in our analysis. Resulting RVs omitting these apertures were improved as can be seen in Figure 3.6. RVs without "bad" apertures are listed in Table B.1. Top panel of Figure 3.6 shows the RVs with apertures 19-30 and the scatter $\sigma = 17 \text{ m} \cdot \text{s}^{-1}$. Bottom panel shows the RVs without "bad" apertures and the scatter $\sigma = 14 \text{ m} \cdot \text{s}^{-1}$.

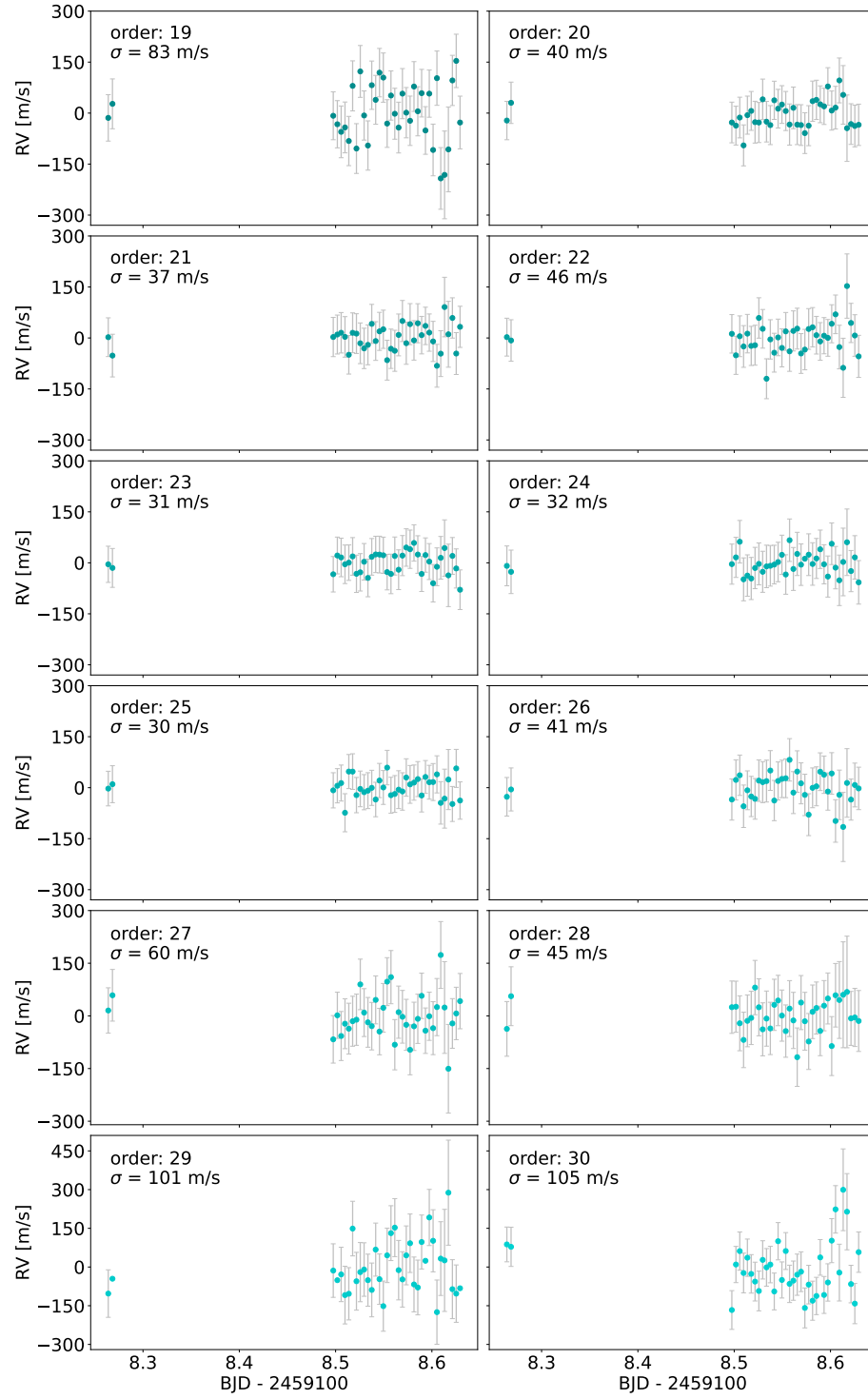


Figure 3.5: Radial velocities of σ Draconis in individual apertures.

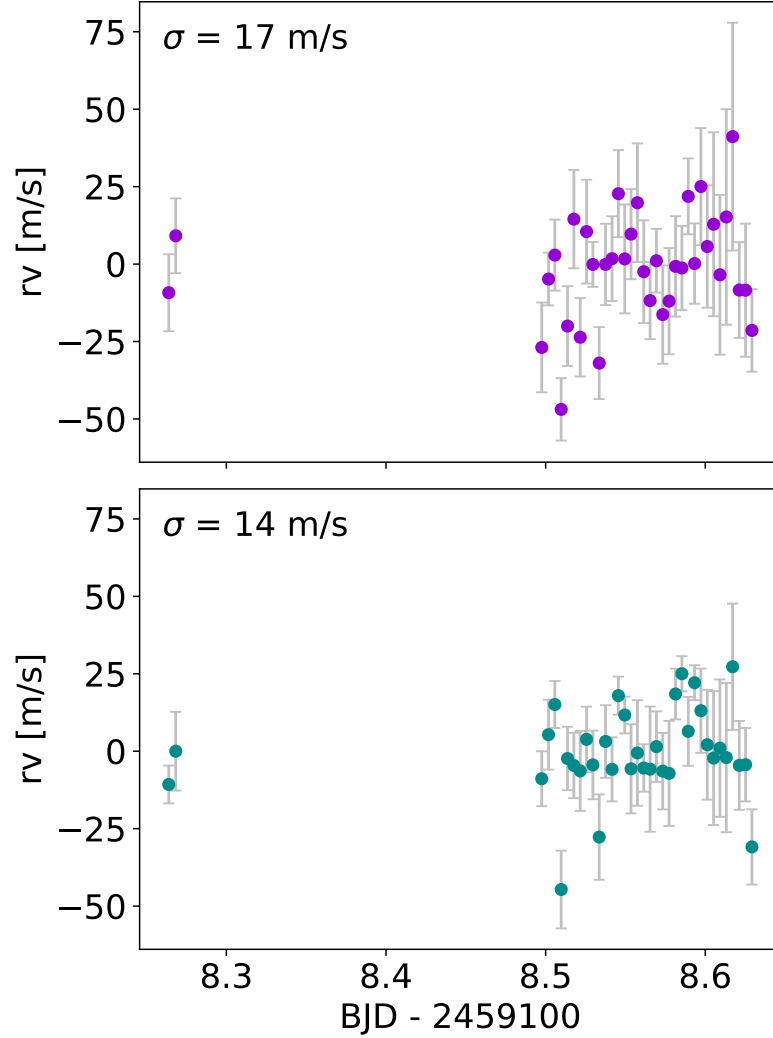


Figure 3.6: Radial velocities of σ Draconis. Plot of total RVs calculated for apertures 19 - 30 (top panel). Plot of total RVs calculated without apertures 19, 27, 29 and 30 (bottom panel).

3.4 Impact of the template

As mentioned earlier, to get the best possible results, the template should have high SNR. To analyze the impact of the SNR of the template on the resulting RVs for the OES data, 12 templates of σ Draconis were taken and 2 templates were made by a combination of some of them. Templates have SNR from 48 to 328. All values are listed in the Table 3.3.

In Figure 3.7, it can be seen that with higher SNR the RVs are more precise but it can be also seen that there is no need of using a combined template and templates with SNR above ≈ 100 give basically the same results. It can be also

seen that two templates (3, 8) are giving worse results. Combined template 1 was made using templates 1 to 8 and combined template 2 was made from a combination of templates 1 to 7 without 3. Values of SNR were obtained in the wavelength range of 6577.8 - 6579.6 Å where no stellar lines of σ Draconis are present.

Another outcome of this analysis was that non-normalised data are giving the best results of RVs so there is no need for normalization of the spectra before the analysis because normalisation introduces an error into the analysis.

Table 3.3: Values of SNR for individual templates.

Template (date)	SNR
1 (October 13th, 2021)	152
2 (October 13th, 2021)	133
3 (October 13th, 2021)	160
4 (October 13th, 2021)	143
5 (October 13th, 2021)	170
6 (October 13th, 2021)	176
7 (September 30th, 2021)	146
8 (October 2nd, 2021)	159
9 (February 24th, 2022)	89
10 (March 9th, 2022)	113
11 (March 9th, 2022)	66
12 (March 9th, 2022)	48
combined template 1	290
combined template 2	328

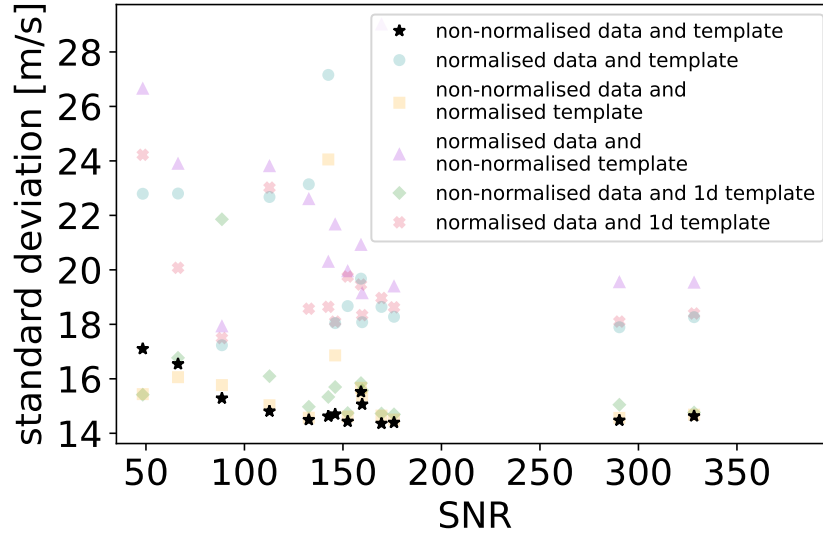


Figure 3.7: Dependency of standard deviation on SNR of the template.

3.4.1 High-resolution template

In *viper*, for better precision of RVs, it is possible to use a high-resolution template taken with a different instrument. In my analysis, I processed data with the OES templates but for 51 Pegasi there is a high-resolution spectrum in the HARPS archive. In Figure 3.8, there are data processed with the OES template, HARPS template and radial velocity curve of 51 Pegasi created using *exostriker* (Trifonov, 2019) with known parameters of the exoplanet obtained from [E05]. Orbital period $P = 4.2308$ days and RV semi-amplitude $K = 55.65 \text{ m} \cdot \text{s}^{-1}$. RVs obtained with the OES template are listed in Table B.2 and RVs obtained with the HARPS template are listed in Table B.3. The RVs from *viper* are relative in respect to the template, thus all data points obtained from *viper* were shifted by $-17 \text{ m} \cdot \text{s}^{-1}$ for OES and also HARPS template. Contrary to expectations, the HARPS template gives worse results than the OES template. 51 Pegasi is the only star from my data set which has a HARPS spectrum, thus, more analysis of stars with a HARPS spectrum is needed.

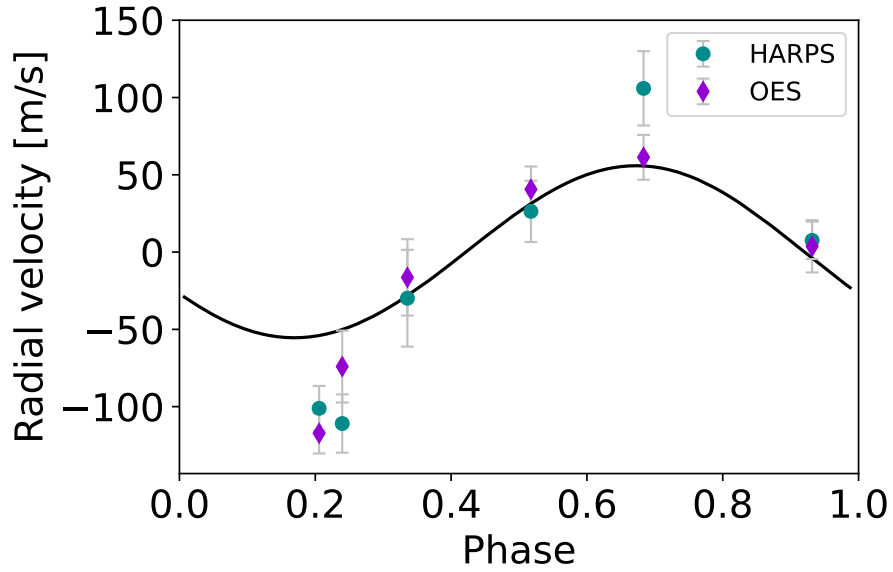


Figure 3.8: Radial velocity curve for 51 Pegasi. Data processed with a template from OES (violet) and HARPS (green) with the radial velocity curve made with the known parameters of the exoplanet using *exostriker* (solid line).

3.5 Observing conditions

In my analysis, I also looked if observation conditions somehow correlate with obtained RVs. As can be seen in Figure 3.9 (top left panel), there could be a correlation between dome temperature and RVs. There is a significant drop in dome temperature and the corresponding change in RVs. The change in temperature in the dome is probably related to a worsening of seeing and thus a smaller SNR. According to the remaining panels, outside temperature, humidity and pressure do not affect the RVs. σ Draconis is the only object from my dataset that was observed through one observing night, therefore, only plots from that observations are shown. For a better understanding of this correlation, more data is needed.

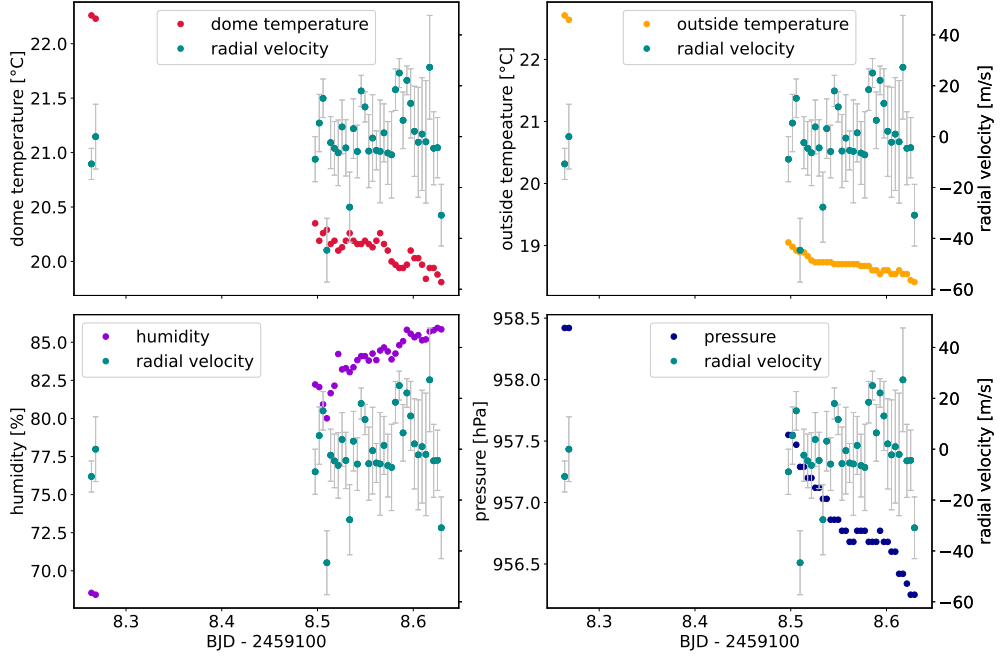


Figure 3.9: Observing conditions for σ Draconis.

3.6 Long-term stability

For the study of the long-term stability of the spectrograph, two targets were used, HD 182572 and HD 10780.

Results for HD 182572 are shown in Figure 3.10 and listed in Table B.4. We see that the scatter over ≈ 175 days is $12 \text{ m} \cdot \text{s}^{-1}$, which means the stability of the spectrograph is very good. The large errors of the last two data points are due to poor SNR.

Results for the second target, HD 10780, are shown in Figure 3.11 and listed in Table B.5. We can see some trend in the data. It does not seem to be an instrumental drift because the RVs of HD 182572 were observed over a similar period. It can be caused by the star itself or it could be a binary system. Another possibility is an exoplanet. More data are needed for the understanding of the trend. In Figure 3.11a can be seen that there is an outlier, Figure 3.11b is after removing this outlier. The scatter after removing the outlier is $\sigma = 42 \text{ m} \cdot \text{s}^{-1}$.

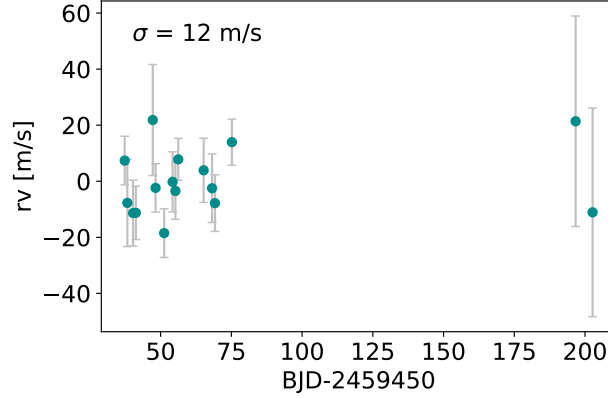


Figure 3.10: RVs of HD 182572.

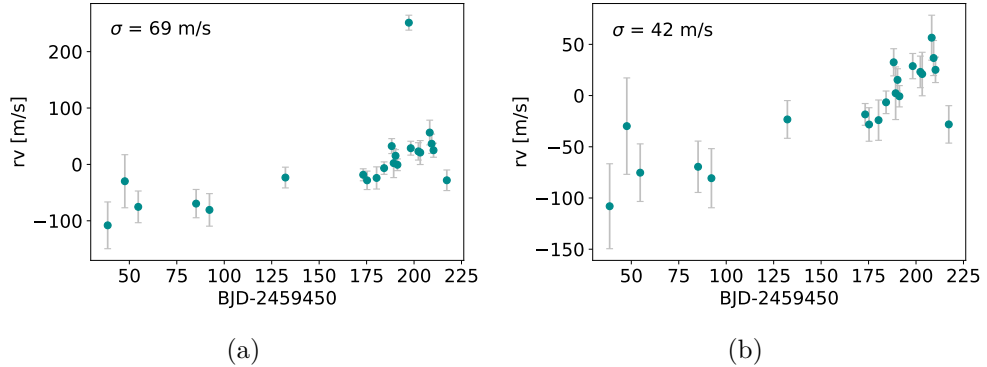


Figure 3.11: RVs of HD 10780. (a) Complete dataset, (b) Outlier removed.

3.7 Cross-correlation with IRAF vs VIPER and iodine cell method

Another tool for the determination of RVs is IRAF. IRAF is using a different method than *viper*. IRAF is using the method of cross-correlation (described in Section 2.3). I analysed data used for *viper* also with IRAF. For the cross-correlation, I used wavelength interval 4000 - 4800 Å. This interval is used because there are no lines from iodine cell or telluric lines and the SNR is still high enough to get precise RVs.

Results are plotted in Figures 3.12, 3.13. It can be seen, that results obtained from IRAF are significantly worse than from *viper*. In Figure 3.13 on the right error bars for σ Draconis are not plotted for better clarity, because errors obtained from IRAF are in the order of $\approx 1 \text{ km} \cdot \text{s}^{-1}$ and errors from *viper* are in the order of $\approx 10 \text{ m} \cdot \text{s}^{-1}$. Overall, data obtained with the iodine cell method gives orders of magnitude better results than the classical cross-correlation method.

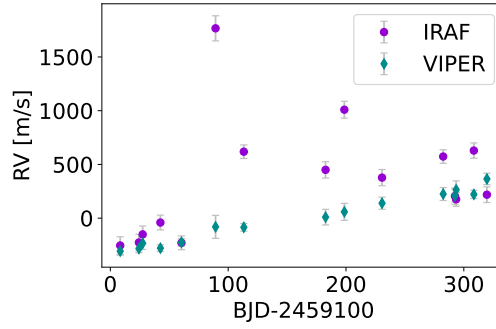


Figure 3.12: The plot of radial velocity for HD 187878 obtained from IRAF and *viper*.

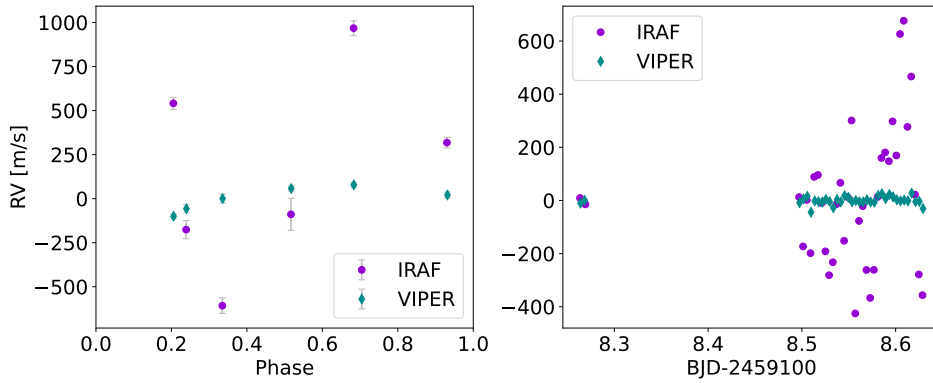


Figure 3.13: The plot of radial velocity for 51 Pegasi (left) and σ Draconis (right) obtained from IRAF and *viper*.

3.8 HD 187878

One of the targets of the Ondřejov observing program is star HD 187878. It is a Red Giant Branch star. The companion of this star was not confirmed yet. RVs obtained using *viper* are shown in Figure 3.14 and listed in Table B.6. These results were added to the results from other observatories. It can be seen in Figure 3.15 that the results obtained with *viper* from Ondřejov observations follow the trend. The scatter of the RVs from Ondřejov is still high and needs to be solved. It may be related to the SNR of the data or some other property of the data. Errors caused by imperfections of *viper* could be ruled out if different software using the same method of RVs calculations would be used. This system is still in the research stage and observations and article is in preparation. From the RV curve shown in Figure 3.14, we can say that this system is composed of a star and a sub-stellar companion.

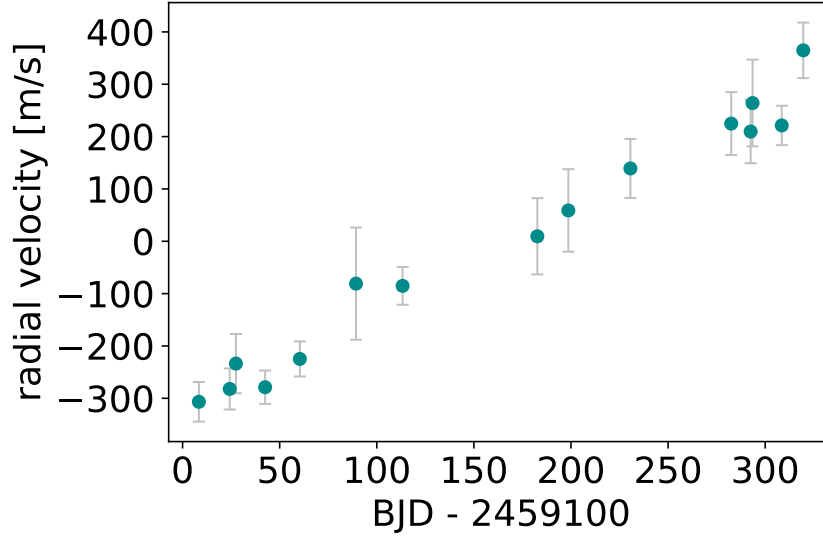


Figure 3.14: Radial velocities of HD 187878 obtained with *viper* using OES data.

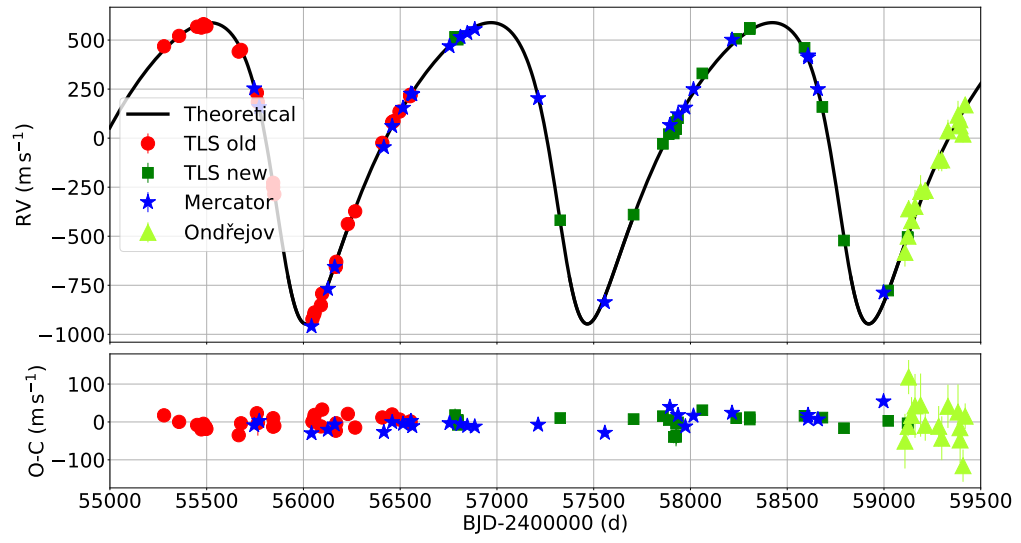


Figure 3.15: Radial velocities of HD 187878 from Ondřejov and other observatories. Ondřejov data in Figure 3.14 are added to the plot. Plot made by Marie Karjalainen.

Discussion and conclusions

In this thesis, I worked with data that were obtained with Ondřejov Echelle Spectrograph (OES) and iodine cell. The main task was to test `viper`, find a good set-up and prove that `viper` works well with OES data.

The best found setting of the `viper` for the OES data is shown in Figure 3.1 and in Table 3.2. First, it was important to find which echelle apertures contain iodine spectrum and also if the apertures are giving reasonable results. My analysis shows that apertures from 19 to 30 have an iodine spectrum. I also found that apertures 19, 29, and 30 do not have enough spectral lines and aperture 27 have too many lines that blend with the stellar spectrum. It results in worse precision of RVs in these apertures. Figure 3.5 shows radial velocities of σ Draconis in individual apertures. For further analysis, I used apertures 20-28 without 27. The improvement in radial velocities precision after excluding the worse apertures is shown in Figure 3.6. For σ Draconis with an apparent magnitude $V = 4.7$ mag it is possible to achieve scatter $\approx 14 \text{ m} \cdot \text{s}^{-1}$ over one night.

The next interest of my study was to find a relation between the SNR of the template and the precision of the RVs. For this task 12 templates of the σ Draconis were taken and 2 combined templates were made, each template has a different quality. These templates are listed in Table 3.3. I used the same data set of observations and the only thing that was changing was the template. The result of this analysis is shown in Figure 3.7. I found that with higher SNR the precision of the RVs is better but templates with SNR above ≈ 100 give almost the same results. In Figure 3.7, it can be also seen that non-normalised data are giving the best results and normalization of the `viper` input data is not needed as it introduces an error into the analysis.

It is often recommended to use a high-resolution template for achieving better precision of the RVs. To test this I used HARPS template for 51 Pegasi as it was the only star from my dataset in the HARPS archive. Results are shown in Figure 3.8. In this figure, the RV curve created in `exostriker` based on the known parameters of the exoplanet is also shown. It can be seen that results obtained with OES template are in better agreement with the curve from `exostriker`.

RVs precision depends on the observing conditions. I looked at the observing

conditions during one observing night of σ Draconis, shown in Figure 3.9. I plotted the dome temperature, outside temperature, humidity and pressure. The correlation between RVs and outside temperature, humidity and pressure was not found but it can be seen that there is a clear correlation between RVs and dome temperature.

For the study of the scatter over a longer period, two targets were used. The first target is HD 182572, the star with $V = 5.2$ mag. RVs are shown in Figure 3.10. Scatter over ≈ 175 days is $12 \text{ m} \cdot \text{s}^{-1}$. In Figure 3.11 results for HD 10780 are shown, HD 10780 is a star with $V = 5.6$ mag. Available data for this target are covering ≈ 200 days. We can see some trend in the data that causes the scatter $42 \text{ m} \cdot \text{s}^{-1}$. The constant RVs of a standard HD 182572 are observed over a similar period as HD 10780. It is the reason why we assume that the trend observed in HD 10780 is of stellar nature, not instrumental. It is possible that the trend is caused by an exoplanet or other body in the system and more data is needed for identification of the origin of this trend.

Another method how to obtain Doppler shifts is the cross-correlation method. To use this method on my dataset I used IRAF. Results are shown in Figures 3.12, 3.13. It can be seen that results from IRAF are significantly worse.

The real performance of **viper** on the OES data was tested on a red-giant star HD 187878. RVs obtained with **viper** are shown in Figure 3.14. Results were added to a plot with results from other observatories, shown in Figure 3.15. RVs from Ondřejov are following the trend in the data.

viper is still under development and more observations and testing needs to be done. During the analysis, it was found that there are still some problems with IP modelling and wavelength solution. The wavelength solution problem is caused by the FTS quality and the IP of OES is changing through the orders. So far, results obtained with **viper** are satisfying and promising and it is clear that the usage of the iodine cell and **viper** is a step in the right direction to get precise RVs.

Bibliography

- [E01]. <http://www.obs-hp.fr/www/archive/elodie-for-dummies.html>.
- [E02]. <https://exoplanets.nasa.gov/>.
- [E03]. <https://stelweb.asu.cas.cz/en/telescope/instrumentation/oes-spectrograph/>.
- [E04]. <http://simbad.cds.unistra.fr/simbad/>.
- [E05]. <http://exoplanet.eu>.
- A. Baranne, D. Queloz, M. Mayor, G. Adrianzyk, G. Knispel, D. Kohler, D. Lacroix, J. P. Meunier, G. Rimbaud, and A. Vin. ELODIE: A spectrograph for accurate radial velocity measurements. *A&AS*, 119:373–390, October 1996.
- R. P. Butler, G. W. Marcy, E. Williams, C. McCarthy, P. Dosanjuh, and S. S. Vogt. Attaining Doppler Precision of 3 M s⁻¹. *PASP*, 108:500, June 1996. doi: 10.1086/133755.
- A. Hatzes. *The Doppler Method for the Detection of Exoplanets*. AAS-IOP astronomy. IOP Publishing Limited, 2019. ISBN 9780750317740.
- W. S. Jacob. On certain Anomalies presented by the Binary Star 70 Ophiuchi. *MNRAS*, 15:228, June 1855. doi: 10.1093/mnras/15.9.228.
- P. Kabáth, M. Skarka, S. Sabotta, E. Guenther, D. Jones, T. Klocová, J. Šubjak, Jiří Žák, M. Špoková, M. Blažek, J. Dvořáková, D. Dupkala, J. Fuchs, A. Hatzes, E. Kortusová, R. Novotný, E. Plávalová, L. Řezba, J. Sloup, P. Škoda, and M. Šlechta. Ondřejov Echelle Spectrograph, Ground Based Support Facility for Exoplanet Missions. *PASP*, 132(1009):035002, March 2020. doi: 10.1088/1538-3873/ab6752.
- P. Koubský, P. Mayer, J. Čáp, F. Žďárský, J. Zeman, L. Pína, and Z. Melich. Ondřejov Echelle Spectrograph - OES. *Publications of the Astronomical Institute of the Czechoslovak Academy of Sciences*, 92:37–43, January 2004.

- Christophe Lovis, Francesco Pepe, François Bouchy, Gaspare Lo Curto, Michel Mayor, Luca Pasquini, Didier Queloz, Gero Rupprecht, Stéphane Udry, and Shay Zucker. The exoplanet hunter HARPS: unequalled accuracy and perspectives toward 1 cm s^{-1} precision. In Ian S. McLean and Masanori Iye, editors, *Society of Photo-Optical Instrumentation Engineers (SPIE) Conference Series*, volume 6269 of *Society of Photo-Optical Instrumentation Engineers (SPIE) Conference Series*, page 62690P, June 2006. doi: 10.1117/12.669991.
- Jack Lubin, Paul Robertson, Gudmundur Stefansson, Joe Ninan, Suvrath Mahadevan, Michael Endl, Eric Ford, Jason T. Wright, Corey Beard, Chad Bender, William D. Cochran, Scott A. Diddams, Connor Fredrick, Samuel Halverson, Shubham Kanodia, Andrew J. Metcalf, Lawrence Ramsey, Arpita Roy, Christian Schwab, and Ryan Terrien. Stellar Activity Manifesting at a One-year Alias Explains Barnard b as a False Positive. *AJ*, 162(2):61, August 2021. doi: 10.3847/1538-3881/ac0057.
- E. Maor. *To Infinity and Beyond: A Cultural History of the Infinite*. 24: The New Cosmology, page 198. Birkhäuser, 1987. ISBN 978-1-4612-5396-9.
- M. Mayor, F. Pepe, D. Queloz, F. Bouchy, G. Rupprecht, G. Lo Curto, G. Avila, W. Benz, J. L. Bertaux, X. Bonfils, Th. Dall, H. Dekker, B. Delabre, W. Eckert, M. Fleury, A. Gilliotte, D. Gojak, J. C. Guzman, D. Kohler, J. L. Lizon, A. Longinotti, C. Lovis, D. Megevand, L. Pasquini, J. Reyes, J. P. Sivan, D. Sosnowska, R. Soto, S. Udry, A. van Kesteren, L. Weber, and U. Weilenmann. Setting New Standards with HARPS. *The Messenger*, 114:20–24, December 2003.
- Michel Mayor and Didier Queloz. A Jupiter-mass companion to a solar-type star. *Nature*, 378(6555):355–359, November 1995. doi: 10.1038/378355a0.
- F. Pepe, S. Cristiani, R. Rebolo, N. C. Santos, H. Dekker, A. Cabral, P. Di Marcantonio, P. Figueira, G. Lo Curto, C. Lovis, M. Mayor, D. Mégevand, P. Molaro, M. Riva, M. R. Zapatero Osorio, M. Amate, A. Manescau, L. Pasquini, F. M. Zerbi, V. Adibekyan, M. Abreu, M. Affolter, Y. Alibert, M. Aliverti, R. Allart, C. Allende Prieto, D. Álvarez, D. Alves, G. Avila, V. Baldini, T. Bandy, S. C. C. Barros, W. Benz, A. Bianco, F. Borsa, V. Bourrier, and Bouchy et al. ESPRESSO at VLT. On-sky performance and first results. *A&A*, 645:A96, January 2021. doi: 10.1051/0004-6361/202038306.
- Michael Perryman. *The Exoplanet Handbook*. Cambridge University Press, 2 edition, 2018. doi: 10.1017/9781108304160.
- I. Ribas, M. Tuomi, A. Reiners, R. P. Butler, J. C. Morales, M. Perger, S. Dreizler, C. Rodríguez-López, J. I. González Hernández, A. Rosich, F. Feng, T. Trifonov, S. S. Vogt, J. A. Caballero, A. Hatzes, E. Herrero, S. V. Jeffers, M. Lafarga, F. Murgas, R. P. Nelson, E. Rodríguez, J. B. P. Strachan, L. Tal-Or, J. Teske, B. Toledo-Padrón, M. Zechmeister, A. Quirrenbach, P. J. Amado, M. Azzaro,

- V. J. S. Béjar, J. R. Barnes, Z. M. Berdiñas, J. Burt, G. Coleman, M. Cortés-Contreras, J. Crane, S. G. Engle, E. F. Guinan, C. A. Haswell, Th. Henning, B. Holden, J. Jenkins, H. R. A. Jones, A. Kaminski, M. Kiraga, M. Kürster, M. H. Lee, M. J. López-González, D. Montes, J. Morin, A. Ofir, E. Pallé, R. Rebolo, S. Reffert, A. Schweitzer, W. Seifert, S. A. Shectman, D. Staab, R. A. Street, A. Suárez Mascareño, Y. Tsapras, S. X. Wang, and G. Anglada-Escudé. A candidate super-Earth planet orbiting near the snow line of Barnard’s star. *Nature*, 563(7731):365–368, November 2018. doi: 10.1038/s41586-018-0677-y.
- O. Struve. Proposal for a project of high-precision stellar radial velocity work. *The Observatory*, 72:199–200, October 1952.
- Doug Tody. The IRAF Data Reduction and Analysis System. In David L. Crawford, editor, *Instrumentation in astronomy VI*, volume 627 of *Society of Photo-Optical Instrumentation Engineers (SPIE) Conference Series*, page 733, January 1986. doi: 10.1117/12.968154.
- Trifon Trifonov. The Exo-Striker: Transit and radial velocity interactive fitting tool for orbital analysis and N-body simulations. *Astrophysics Source Code Library*, record ascl:1906.004, June 2019.
- Jeff A. Valenti, R. Paul Butler, and Geoffrey W. Marcy. Determining Spectrometer Instrumental Profiles Using FTS Reference Spectra. *PASP*, 107:966, October 1995. doi: 10.1086/133645.
- P. van de Kamp. Alternate dynamical analysis of Barnard’s star. *AJ*, 74:757–759, August 1969. doi: 10.1086/110852.
- M. Wenger, F. Ochsenbein, D. Egret, P. Dubois, F. Bonnarel, S. Borde, F. Genova, G. Jasiewicz, S. Laloë, S. Lesteven, and R. Monier. The SIMBAD astronomical database. The CDS reference database for astronomical objects. *A&AS*, 143:9–22, April 2000. doi: 10.1051/aas:2000332.
- Robert A. Wittenmyer, Michael Endl, William D. Cochran, Artie P. Hatzes, G. A. H. Walker, S. L. S. Yang, and Diane B. Paulson. Detection Limits from the McDonald Observatory Planet Search Program. *AJ*, 132(1):177–188, July 2006. doi: 10.1086/504942.
- Mathias Zechmeister, Jana Köhler, and Sireesha Chamarthi. *viper: Velocity and IP Estimator*, August 2021.
- Miroslav Šlechta. Modernizace 2m perkova dalekohledu v ondřejově. *Astropis*, 2020:12–15, 3 2020.
- All internet sources ([E01] - [E05]) were up to date 16.5.2022.

APPENDIX A

Input data for viper

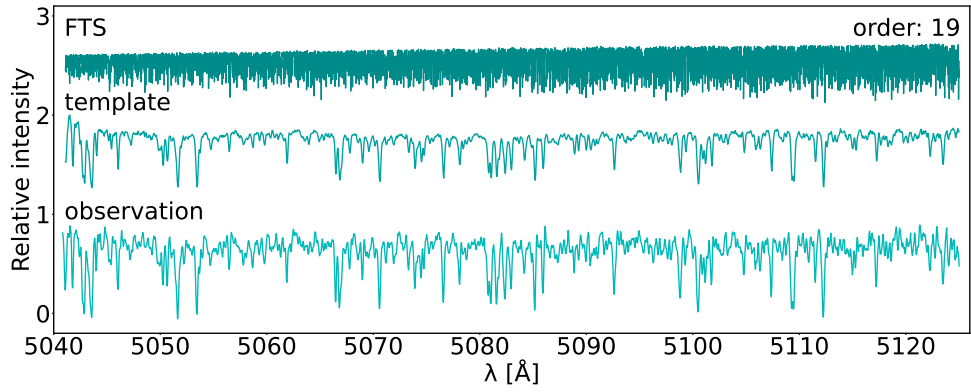


Figure A.1: Spectra of aperture 19 of iodine cell, σ Draconis template and σ Draconis observation.

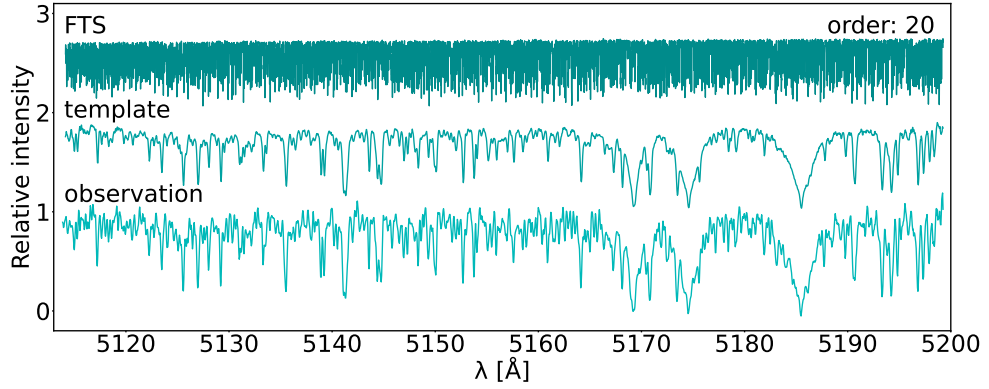


Figure A.2: Spectra of aperture 20 of iodine cell, σ Draconis template and σ Draconis observation.

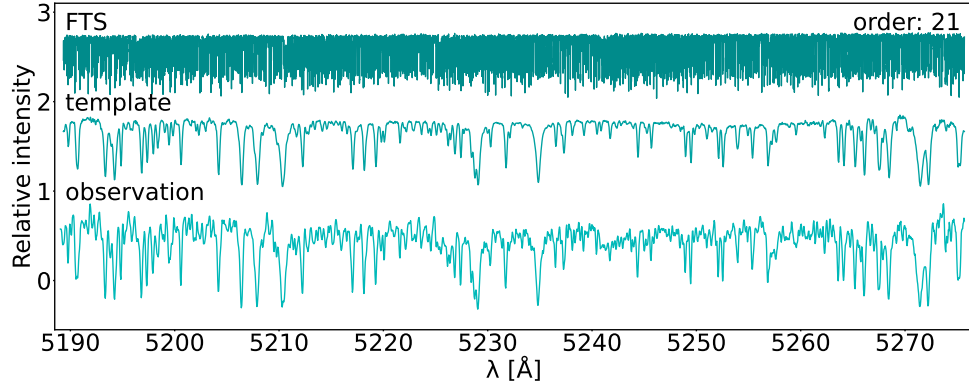


Figure A.3: Spectra of aperture 21 of iodine cell, σ Draconis template and σ Draconis observation.

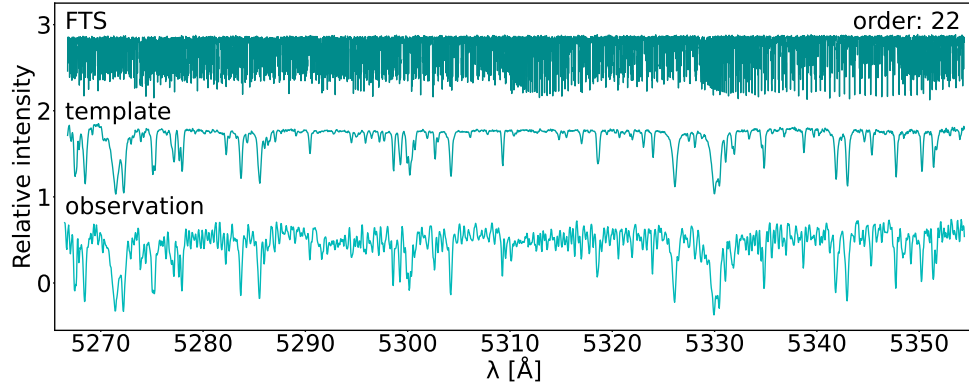


Figure A.4: Spectra of aperture 22 of iodine cell, σ Draconis template and σ Draconis observation.

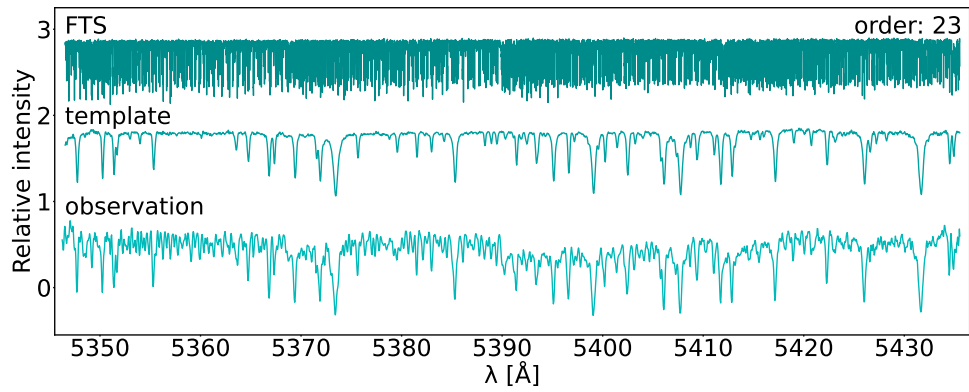


Figure A.5: Spectra of aperture 23 of iodine cell, σ Draconis template and σ Draconis observation.

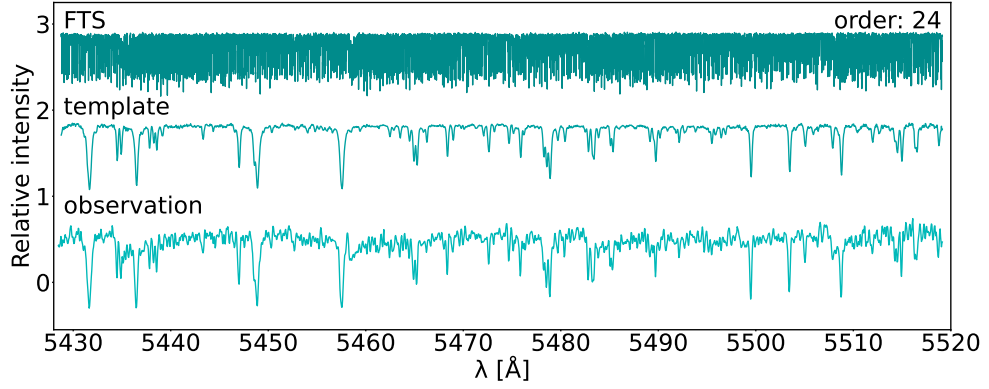


Figure A.6: Spectra of aperture 24 of iodine cell, σ Draconis template and σ Draconis observation.

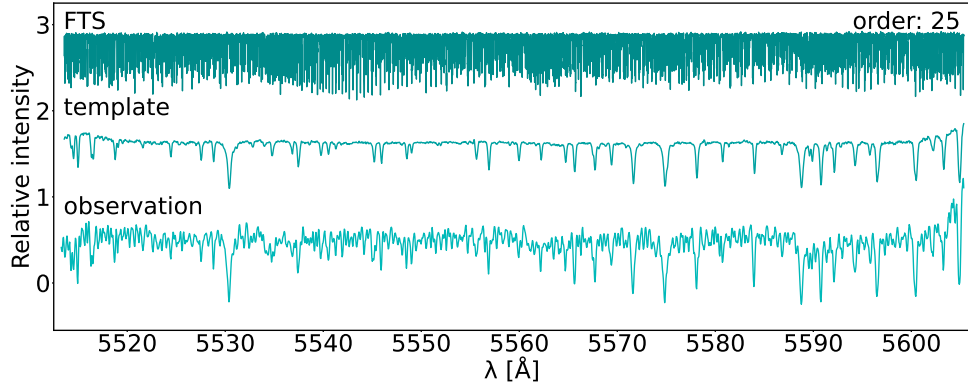


Figure A.7: Spectra of aperture 25 of iodine cell, σ Draconis template and σ Draconis observation.

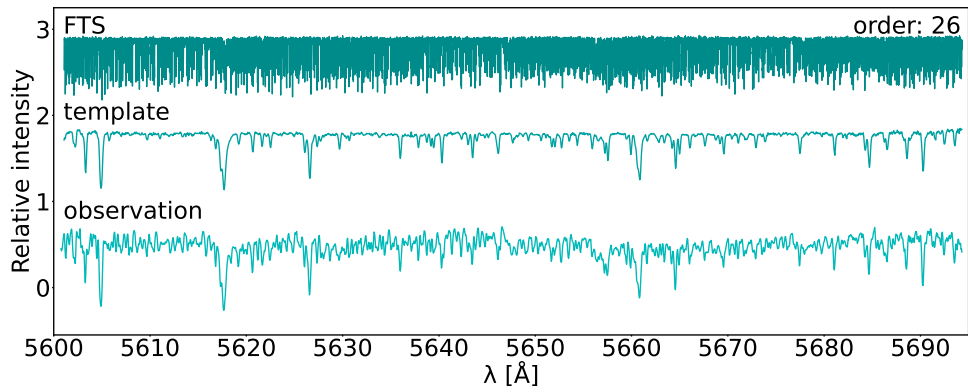


Figure A.8: Spectra of aperture 26 of iodine cell, σ Draconis template and σ Draconis observation.

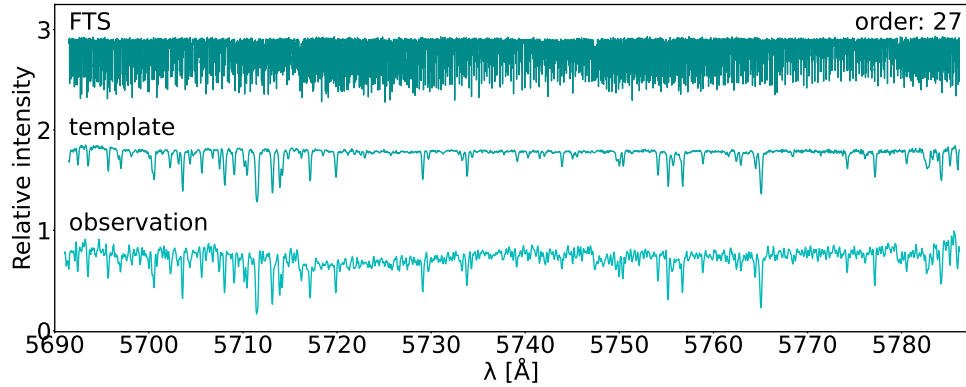


Figure A.9: Spectra of aperture 27 of iodine cell, σ Draconis template and σ Draconis observation.

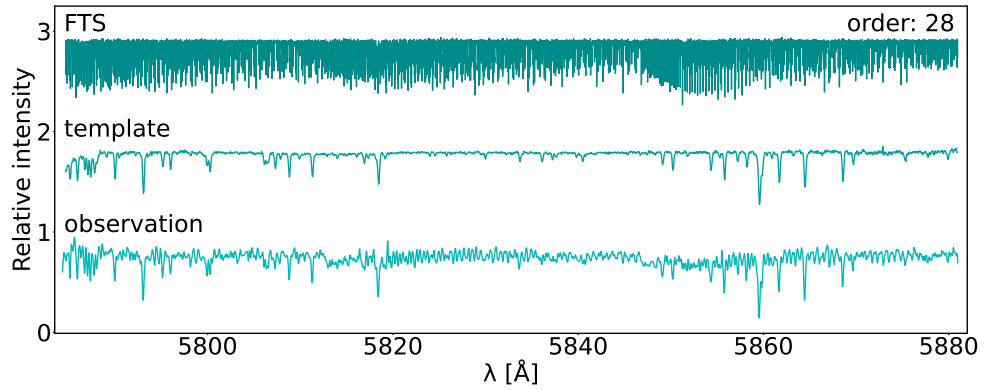


Figure A.10: Spectra of aperture 28 of iodine cell, σ Draconis template and σ Draconis observation.

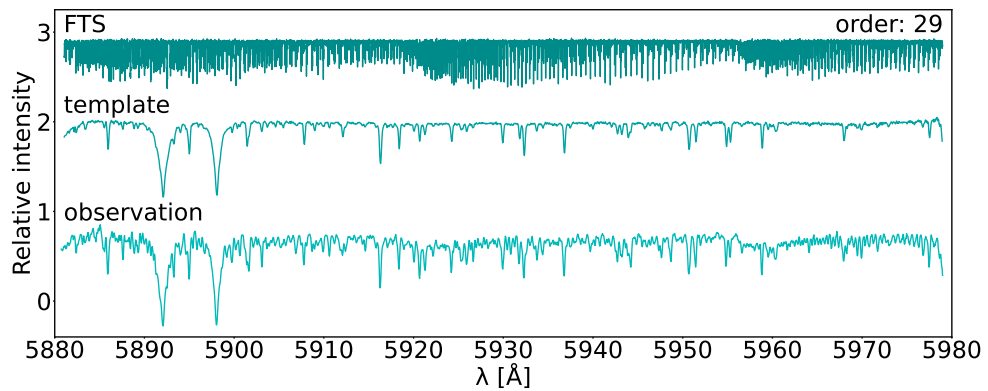


Figure A.11: Spectra of aperture 29 of iodine cell, σ Draconis template and σ Draconis observation.

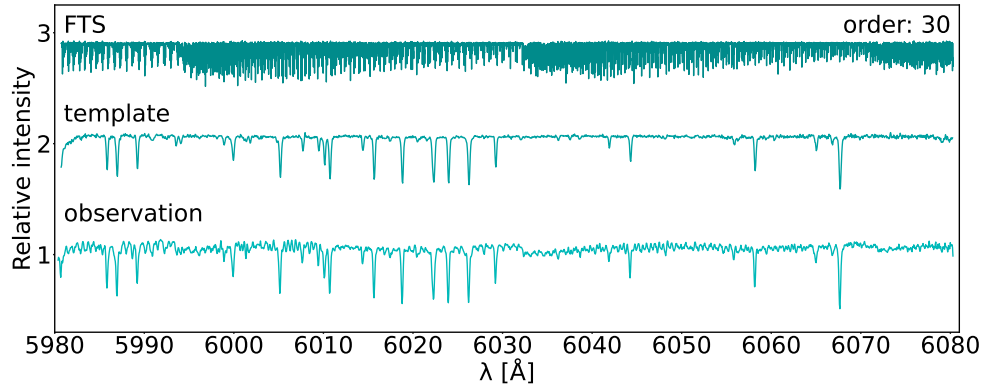


Figure A.12: Spectra of aperture 30 of iodine cell, σ Draconis template and σ Draconis observation.

APPENDIX B

Radial velocity

B.1 σ Draconis

Table B.1: Radial velocities of σ Draconis

BJD	RV [m/s]	RV error [m/s]
2459108.26393	-10.27	6.26
2459108.26830	0.47	12.51
2459108.49756	-8.41	8.50
2459108.50181	5.81	10.81
2459108.50578	15.54	7.84
2459108.50975	-44.18	12.53
2459108.51372	-1.89	10.09
2459108.51769	-4.14	10.37
2459108.52166	-5.90	12.37
2459108.52563	4.29	10.44
2459108.52960	-3.96	11.70
2459108.53357	-27.26	13.55
2459108.53754	3.60	11.77
2459108.54161	-5.38	10.44
2459108.54558	18.42	5.50
2459108.54955	12.15	5.99
2459108.55352	-5.22	14.54
2459108.55749	-0.09	17.10
2459108.56146	-4.95	7.99
2459108.56543	-5.32	20.63
2459108.56940	1.95	10.99
2459108.57337	-5.97	12.03
2459108.57734	-6.69	17.06
2459108.58140	18.94	8.43
2459108.58537	25.47	5.24
2459108.58934	6.88	11.58
2459108.59331	22.58	5.45
2459108.59728	13.54	13.52
2459108.60125	2.57	18.18
2459108.60522	-1.75	21.46
2459108.60919	1.46	22.23
2459108.61316	-1.58	23.90
2459108.61713	27.74	20.38
2459108.62130	-4.11	14.37
2459108.62527	-3.88	11.84
2459108.62924	-30.43	11.90

B.2 51 Pegasi

Table B.2: Radial velocities of 51 Pegasi obtained with OES template.

BJD	Phase	RV [m/s]	RV error [m/s]
2459487.29014	0.93164	20.73	16.91
2459488.44950	0.20567	-100.20	13.07
2459490.47066	0.68339	78.33	14.50
2459497.46099	0.33565	0.62	24.72
2459498.23072	0.51758	57.59	14.81
2459501.28587	0.23971	-57.07	23.28

Table B.3: Radial velocities of 51 Pegasi obtained with HARPS template.

BJD	Phase	RV [m/s]	RV error [m/s]
2459487.29014	0.93164	24.57	12.11
2459488.44950	0.20567	-84.07	14.50
2459490.47066	0.68339	122.92	24.04
2459497.46099	0.33565	-12.86	31.31
2459498.23072	0.51758	43.35	19.84
2459501.28587	0.23971	-93.92	18.87

B.3 HD 182572

Table B.4: Radial velocities of HD 182572.

BJD	RV [m/s]	RV error [m/s]
2459487.31193	7.37	8.70
2459488.24278	-7.73	15.57
2459490.26191	-11.34	11.73
2459491.24185	-11.28	9.53
2459497.23059	21.85	19.81
2459498.22192	-2.37	8.65
2459501.24687	-18.50	8.69
2459504.23043	-0.22	10.72
2459505.23092	-3.46	10.11
2459506.22963	7.82	7.50
2459515.20897	3.90	11.46
2459518.18831	-2.50	12.22
2459519.21518	-7.81	10.09
2459525.18725	13.95	8.23
2459646.68916	21.40	37.56
2459652.67941	-11.09	37.23

B.4 HD 10780

Table B.5: Radial velocities of HD 10780.

BJD	RV [m/s]	RV error [m/s]
2459488.59055	-108.05	41.47
2459497.61990	-29.83	47.07
2459504.68529	-75.28	28.12
2459535.17622	-69.52	25.08
2459542.20750	-80.67	28.86
2459582.22303	-23.30	18.41
2459623.21016	-18.40	10.62
2459625.25680	-28.23	16.36
2459630.26158	-24.00	19.69
2459634.22212	-6.58	11.04
2459638.23144	32.49	13.25
2459639.26582	2.27	25.70
2459640.25798	15.32	10.87
2459641.24015	-0.66	10.39
2459647.24955	251.38	13.25
2459648.26459	28.76	12.33
2459652.28048	23.12	15.41
2459653.26180	21.03	21.24
2459658.25772	56.51	21.95
2459659.27231	36.66	17.13
2459660.25991	25.13	12.43
2459667.26147	-28.14	18.27

B.5 HD 187878

Table B.6: Radial velocities of HD 187878.

BJD	RV [m/s]	RV error [m/s]
2459108.39906	-306.72	37.84
2459124.27691	-282.18	39.26
2459127.46594	-233.70	56.54
2459142.50838	-278.82	31.86
2459160.37835	-224.77	33.54
2459189.30555	-80.96	107.19
2459213.29962	-85.22	36.06
2459282.67838	9.51	72.85
2459298.63026	58.92	78.88
2459330.59487	139.16	56.40
2459382.50047	224.81	60.12
2459392.51321	209.69	60.53
2459393.49380	264.13	82.91
2459408.52982	221.33	37.64
2459419.60153	364.82	53.09